Harmonic Generation in Microwave Microplasma

A thesis submitted by

Stephen Parsons

In partial fulfillment of the requirements for the degree of

Master of Science

in

Electrical Engineering

Tufts University

May 2016

Advisor: Professor Jeffrey Hopwood

Abstract

Harmonic generation in microplasmas is explored theoretically and experimentally, and then compared with a 2D fluid model. A microstrip split ring resonator with 150 μm gap is designed to provide a microplasma source at around 1 GHz. Electrode area asymmetry is a known factor in harmonic generation in plasmas and is explored. Gas pressures of 0.2 Torr to 760 Torr in argon with power levels of 0.5 to 3 W are examined. Experimental results show third harmonic output of greater than 10 mW is achieved with 3 W of net input power in 0.3 Torr of argon and with asymmetric electrode areas. Experimental results of a microstrip split ring resonator in a frequency mixer configuration are also shown. Fluid model simulations of Gregorio reveal that the small electrode area of an asymmetric discharge forces a higher voltage, which strongly modulates the sheath width and creates hot electrons. A nonlinear voltage-capacitance relationship, as well as hot electrons causing large conduction current spikes, are the sources of harmonic current in the plasma. Results of experiments and fluid model simulations are compared and are found to compare reasonably well.

Table of Contents

List of Figures

Harmonic Generation in

Microwave Microplasma

1. Introduction

Applications of terahertz radiation (loosely defined as 100 GHz to 10 THz) are of great interest to the medical, scientific and defense industries. Terahertz imaging has the advantage of high resolution without ionization of tissue [1], and therefore it may eliminate the harmful effects of x-rays. Terahertz spectroscopy has found applications in chemistry and biochemistry to study samples that are opaque in other frequency ranges [2]. In addition to imaging, terahertz radiation has also been used to study materials in high magnetic fields. However, the advancement of these technologies have been hampered by insufficient power output from current devices.

The main two sources of terahertz power, solid-state semiconductor devices and photonics, both suffer from low output power in the so-called THz gap (lack of available power at around 1 THz). Figure 1.1 shows the currently available power as a function of frequency for the various types of THz sources. Solid-state electronics, which dominate in the lower half of the THz range (< 1 THz), suffer from electrical breakdown at high power and reduced power output at THz frequencies. Photonic devices, which dominate in the upper region of the THz range (> 1 THz), usually require cryogenic cooling and only offer short pulses of THz power. The new development of intense microplasma technologies (which are similar in operation to semi-conductors) offers a viable substitute for semiconductor materials because they do not suffer from breakdown at high power and may have significantly greater carrier mobility and frequency response.

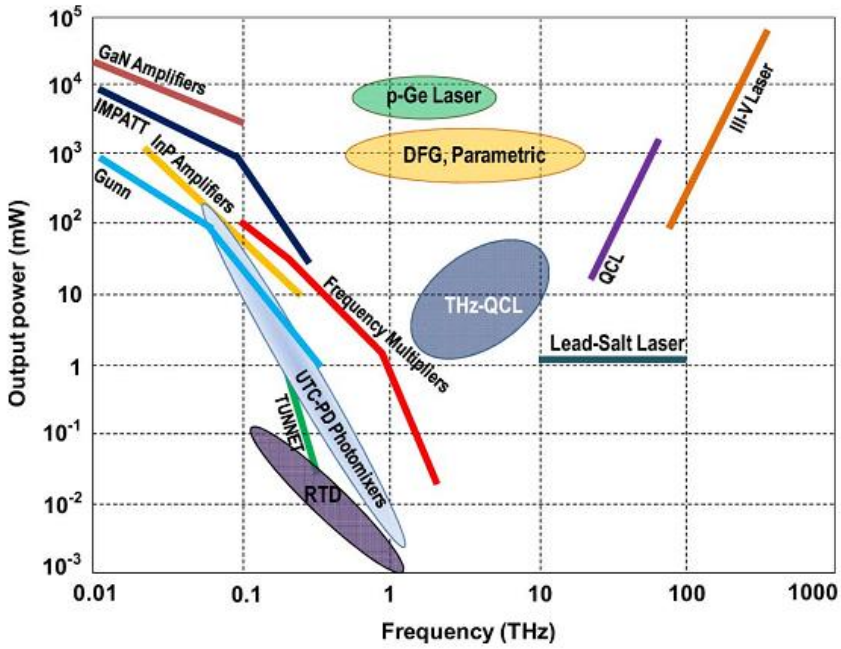

Figure 1.1. Terahertz sources as a function of frequency. Solid lines represent conventional sources of THz and comprise the vast majority of sources [3].

Research into using conventional-scale plasma for harmonic generation and frequency mixing occurred in the 1960's [4]–[7]. Conventional-scale plasmas refer to plasmas on the order 1 mm or greater, at low pressure (typically 1 Torr or less), and power densities less than 10 W/cm^3. For contrast, the microplasmas realized during the course of this research typically have dimensions of less than 1 mm (depending on pressure), pressures ranging from 0.3 Torr to atmospheric pressure, and power densities ranging from 1 W/cm^3 to1.5 kW/cm^3. The early efforts to generate harmonics were successful; however, they were abandoned due to the emergence of semiconductor technologies.

Recent advancements in microstrip based microplasma sources [8]–[12] as well as semiconductor devices reaching their physical limitations in power and voltage [13]–[15] lead us to revisit plasmas, which are known to have non-linear behavior [16]-[17], to potentially further the advancement of harmonic based frequency multipliers. The increase in power density, electron density, and gas pressure as compared to the conventional plasmas of the 1960's allows microplasmas to more readily compete with semiconductor materials. In addition, plasmas have higher electron mobility as compared with semiconductor materials, potentially allowing much higher frequency operation.

Observation of harmonic generation has recently been reported in metamaterial sustained plasmas [18], [19]. Metamaterials are engineered materials that exhibit electrical and magnetic properties of those not found in nature. In these studies, the creation of harmonics is not the expressed goal of the devices, and only second harmonics are reported. Other recent studies involve harmonic generation via the interactions between plasmas and lasers [20]–[23].

The subject of this thesis is to explore the nonlinear nature of microplasmas as they relate to the generation of harmonics (integer multiples of the applied fundamental frequency). The generation of harmonics and their efficient extraction form the basis for frequency multiplier technologies, which dominate current THz sources below 1 THz. An additional investigation into the mixing properties of microplasmas is also presented.

In the work presented here, I will develop equations that predict the existence of second harmonics in plasma using a simplified matrix sheath model. These expressions show that second harmonic generation greatly depends on electrode area asymmetry. I then show the design and simulation of a microstrip split ring resonator (SRR) plasma source that was first reported in 2003 by [9]. The SRR is designed in the microwave frequency range. While I do not expect the same level of microwave harmonic generation efficiency as with current semi-conductor based devices, this is an important first step to understanding the basic science before continuing on into the terahertz frequency regime.

I will also present experimental results of the dependence of harmonic generation on electrode asymmetry, net input power, and gas pressure. Finally, I compare the experimental results with results of a fluid model (developed by Gregorio) in conjunction with a circuit model simulation. This comparison serves to both validate the fluid model and to give a better understanding of the mechanisms involved in harmonic generation.

2. Current Multiplier Technologies

Solid-state frequency multipliers are the most commonly used technology for generating power at and below 1 THz [3]. The most common types of multiplier technologies are Schottky barrier diode and Heterostructure Barrier Varactor (HBV). These technologies operate by generating harmonics through the use of a solid-state non-linear element (*e.g.*, diodes) and efficiently extracting the desired frequency.

2.1. Schottky Barrier Diode Multipliers

Frequency multipliers based on Schottky barrier diodes exploit the non-linear reactive and resistive natures of the diode to create harmonics of an applied pump frequency [24]. A simplified circuit model of a Schottky barrier diode for use a low frequency is shown in Figure 2.1 (a). This model includes the parasitic series resistance, R_s, as well as a diode element (which is represented as a voltage dependent current source) in parallel with a voltage dependent capacitance. This simplified model works well at low frequency, but at higher frequencies, additional parasitics must be considered to properly model the Schottky diode. Figure 2.1 (b) includes these additional parasitic components.

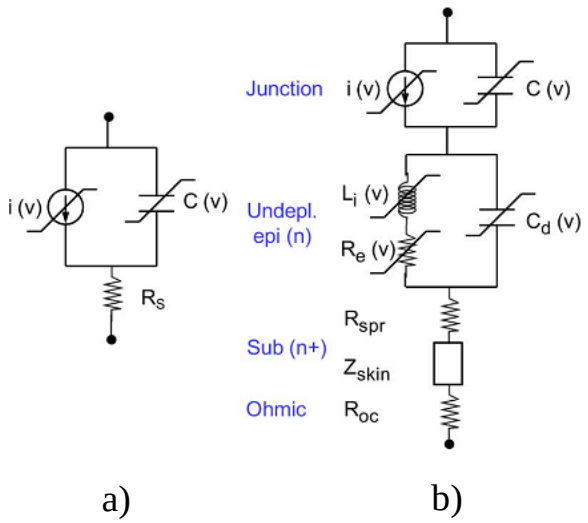

Figure 2.1. (a) Simplified model of Schottky barrier diode at low frequency. (b) Improved model of Schottky barrier diode for use at Terahertz frequencies [25].

At low frequencies, harmonic generation is accomplished by applying a fundamental voltage to the diode and extracting the desired harmonic at the output

of the diode by means of a filter. At high frequencies, such as THz, a more sophisticated method is required due to the need to use waveguide components for efficiency reasons. A typical Schottky barrier diode multiplier in waveguide is shown in Figure 2.2. Power at the fundamental is applied through a waveguide input and the electric field is coupled to the Schottky diode via a patch antenna within the input waveguide, which directs the fundamental current to the diode. Harmonic power is extracted by the use of a second patch antenna, which radiates the power at the desired harmonic into an output waveguide. Filtering and impedance matching is also included for maximum efficiency.

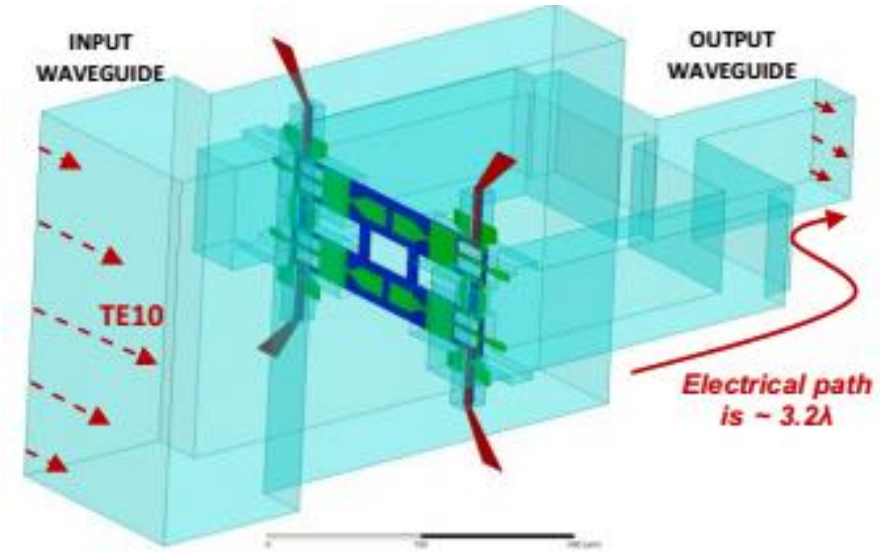

Figure 2.2. Typical Schottky barrier diode frequency multiplier with dual output path and a power combiner [26].

Recent works of Schottky diode frequency multipliers include a 105-120 GHz frequency tripler producing nearly 200 mW with ~ 25% efficiency [27]; a 840-900 GHz frequency multiplier chain delivering ~1.4 mW with ~ 2.4% efficiency

[28]. The dramatic drop off in output power and efficiency from 100 GHz to 900 GHz is in due to the limitations imposed by semiconductor materials. Higher output requires higher voltage amplitudes across the diode capacitance and is effected by three main factors [3]. First, the breakdown voltage, V_b, limits the voltage that can be applied across the diode, which affects the amount of non-linearity. Second, at higher frequencies, the carrier mobility is reduced in the diode junction, which limits the current. Third, voltage is limited by the input power for a given diode capacitance, which is affected by the size of the diode, which can only be reduced to a certain point. It is in these areas and plasma based multipliers may be able to improve upon semiconductor based designs.

2.2. Heterostructure Barrier Varactor Multipliers

Heterostructure barrier varactors (HBV), which were first introduced in 1989 [29], are symmetric devices composed of high bandgap semiconductor surrounded by moderately doped semiconductor. HBV's have symmetric capacitance-voltage and anti-symmetric current-voltage characteristics, Figure 2.3, which produce odd-order harmonics [30]–[32]. When a AC voltage is applied across the HBV, the high bandgap semiconductor material is a barrier to charge carriers, which then accumulate and cause a depletion of carriers in the low bandgap region of the HBV. This accumulation and depletion is the source of the non-linear C-V relationship [33].

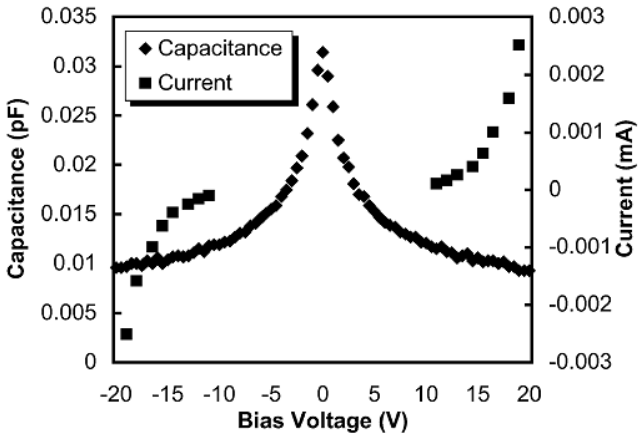

Figure 2.3. Representative example of the C-V and I-V characteristics of an HBV device [13].

HBV's have an advantage over Schottky diodes as they do not require a DC bias, since the capacitance modulations is centered at zero-bias [34]. An additional advantage of HBV's over Schottky diodes are the HBV's ability to withstand much higher input voltage due to the stacking of several barrier layers [33]. This higher input voltage allows for higher output power capabilities. However, these advantages have only been realized at the lower end of the THz region [3].

HBV multipliers are constructed similarly to that of Schottky barrier diode multipliers. Input power at the fundamental is applied via waveguide to a microstrip transition with a lowpass filter. A voltage is formed across the HBV diode, which produces harmonics. The signal is then passed through a matching network and a microstrip to waveguide transition to the output waveguide. Figure 2.4 depicts a typical HBV multiplier setup.

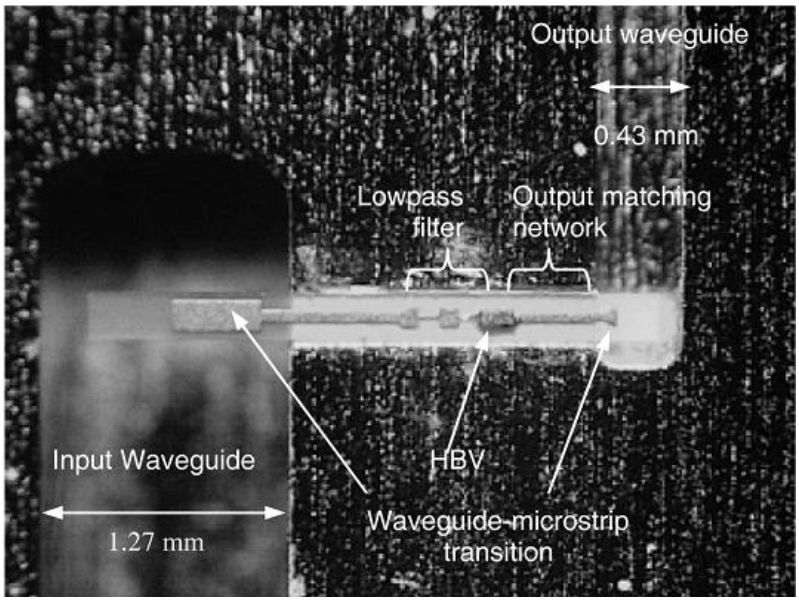

Figure 2.4. Planar HBV diode mounted on microstrip coupled between and input and output waveguide [34].

Recent reports of HBV multipliers include a W-band (90-110 GHz) tripler with a maximum output power of 22.6 dBm (184 mW) with 23% efficiency [35], a 175 GHz quintupler with 60 mW of output power and 6.3% efficiency [36], and a 282 GHz Tripler with 31 mW output power and 7%. efficiency [37]. At higher frequency, a 474 GHz quintupler with a peak output of 2.8 mW operating at 0.75% efficiency has been recently reported [38]. These reported devices show a steep decline in efficiency as compared to Schottky diode based multipliers. However, HBV devices exhibit higher output power capabilities in the low THz range, and so may be used as a high power first stage in multiplier chains incorporating Schottky diodes.

3. Plasma Model with Non-Linear Sheaths

For microwave-drive microplasmas used for this research, I will employ a capacitively-coupled homogeneous plasma model as a first order approximation for the dynamics of the sheaths and bulk of the microplasma. The derivation of this model can be found in Chapter 11 of [39] and is summarized here. The results in [39] show a linear bulk admittance as well as linear admittance across the two sheaths combined. I will make modifications to the displacement current derivation to show the non-linear nature of the resulting sheath voltages when asymmetric discharge electrodes sizes are used.

The results that follow show that for asymmetric discharge electrodes with an applied sinusoidal current, the combined voltage that develops across the two sheaths contain not only the fundamental frequency of the applied current, but also the second harmonic and a DC offset as well. While the experimental results of these devices show additional harmonics, the model here provides some basic physical insight into the potential for harmonic generation using a microplasma.

3.1. Model Configuration and Assumptions

The configuration for this model is shown in Figure 3.1. Two parallel plates with cross sectional areas A_a and A_b are separated by a distance l filled with a gas with neutral gas density n_g. A sinusoidal current $I_{rf}(t)$ is applied to the plates resulting in voltage $V(t)$ across the gap and the formation of a plasma (with length d) with a matrix sheath ($n_i \approx n_e$ in bulk and $n_e \approx 0$ in the sheaths, where n_e and n_i are the electron and ion densities) with average sheath widths of s_a and s_b and

instantaneous sheath widths of $s_a(t)$ and $s_b(t)$. Typically, the average sheath widths s_a and s_b are much smaller than the distance between the plates, l.

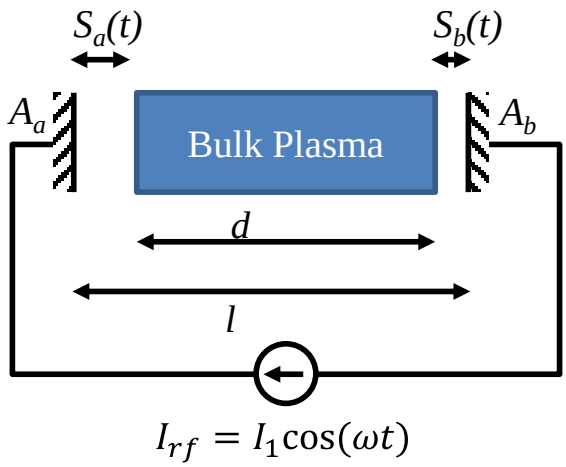

Figure 3.1. Schematic of a parallel plate capacitive coupled discharge

For ease of analysis, the following simplifying assumptions are made [39]:

a. Ions respond to time-averaged potentials only. This assumption is valid provided the square of the ion plasma frequency, ω_{pi}, is much less than the square of the applied frequency ω:

$$\omega_{pi}^2 \ll \omega^2.$$

b. Electrons respond to the instantaneous potential and carry the discharge current. Validity requires,

$$\omega_{pe}^2 \gg \omega \left(1 + \frac{\nu_m^2}{\omega^2}\right)^{\frac{1}{2}},$$

where ω_{pe} is the electron plasma frequency and ν_m is the electron-neutral frequency for momentum transfer.

c. Within the sheaths, the electron density is zero (matrix sheath model).

d. One dimensional electrostatic solution to Maxwell's equations. Valid when the length of the plasma is much smaller than the square-root of the electrode area, $l \ll \sqrt{A}$. See [39] for additional considerations for this approximation.

e. Uniform and constant ion density in the sheath and bulk plasma regions, $n_i(r, t) = n =$ constant. Quasi-Neutral in bulk region, $n_i \approx n_e$. Ion and electron density profiles are depicted in Figure 3.2.

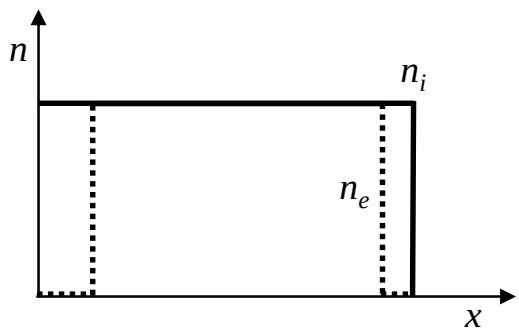

Figure 3.2. Electron and Ion density profiles for matrix sheath plasma model

Using these assumptions, equations for bulk plasma and sheath admittances are derived in the following sections, along with an associated circuit model. In addition, the voltage developed across the bulk plasma and across each sheath is shown, as well as the combined voltage across the entirety of the plasma. This developed voltage will show the generation of harmonics due the asymmetry induced by varying the ratio of the two discharge electrode areas.

3.2. Bulk Plasma Admittance

The bulk plasma of a capacitive discharge is modeled simply as a lossy parallel plate capacitor with the admittance given by

$$Y_p = \frac{j\omega\epsilon_p A}{d} \tag{3.1}$$

where the plasma dielectric constant, ε_p, is given by [39]

$$\epsilon_p = \epsilon_0 \left[1 - \frac{\omega_{pe}^2}{\omega(\omega - j\nu_m)}\right] \tag{3.2}$$

The bulk plasma length, d, is given by, $d \approx l - 2\bar{s}$, and can be assumed to be constant and therefor independent of time. This assumption is valid given that $l \gg \bar{s}$.

Inserting equation (3.2) into (3.1) and simplifying, the bulk plasma admittance is re-written as

$$Y_p = j\omega C_0 + \frac{1}{j\omega L_p + R_p} \tag{3.3}$$

where the vacuum capacitance, C_0, the plasma inductance, L_p, and the plasma resistance, R_p, are given by

$$C_0 = \frac{\epsilon_0 A}{d}, \tag{3.4}$$

$$L_p = \omega_{pe}^{-2} C_0^{-1}, and \tag{3.5}$$

$$R_p = \nu_m L_p. \tag{3.6}$$

The bulk plasma admittance, Y_p, is represented by the series combination of the plasma inductance and the plasma resistance in parallel with the vacuum

capacitance as illustrated in Figure 3.7. The applied sinusoidal current, $I_{rf}(t)$ that flows through this network produces a voltage across the bulk plasma,

$$V_p(t) = \frac{I_{rf}(t)}{Y_p} = \Re\left(\tilde{V}_p e^{j\omega t}\right) \tag{3.7}$$

where $\tilde{V}_p = \tilde{I}_{rf}/\tilde{Y}_p$ is the complex voltage amplitude across the plasma. In this simplified model, the voltage developed across the bulk plasma is linear with the applied current and as such does not produce harmonics.

3.3. Sheath Admittance

Due to the lack of electrons within the sheath, see assumption c, the current that flows through the sheath is almost entirely displacement current. However, a small ion current flows between the plasma and the discharge plate as well as a countering electron current when the sheath collapses.

To solve for the displacement current across the sheath we start with the matrix model of a constant ion density, n_i, and zero electron density, n_e, and integrate Poisson's equation to obtain an expression for the electric field E,

$$E(x,t) = -\int_x^{s_a(t)} \frac{en_i}{\epsilon_0} dx = \frac{en_i}{\epsilon_0}[x - s_a(t)] \tag{3.8}$$

for sheath a, and a similar equation for sheath b.

The boundary condition is $E \approx 0$ at the sheath/plasma boundary, which is valid given that there is no surface charge at the boundary (E is continuous) and the electric field within the plasma is much smaller than within the sheaths.

The displacement current though sheath a is given as

$$I_{ap}(t) = \epsilon_0 A_a \frac{\partial E}{\partial t} \tag{3.9}$$

Inserting the electric field from equation (3.8) into the displacement current in equation (3.9) yields

$$I_{ap}(t) = -\epsilon_0 n_i A_a \frac{d}{dt} s_a(t) \tag{3.10}$$

for sheath *a*. By equation (3.10), sheath *a* oscillates linearly with the applied current.

Assuming the conduction current is small as compared to the displacement current, we can set $I_{ap}(t) = I_{rf}(t) = I_1 \cos(\omega t)$ and insert into equation (3.10) and integrate to obtain an expression for the width of sheath *a*,

$$s_a(t) = \bar{s}_a - s_{0a} \sin(\omega t), \tag{3.11}$$

where the average sheath width, $\bar{s}_a$, is a constant and the sheath width amplitude, s_{0a}, is defined as

$$s_{0a} = \frac{I_1}{e n_i \omega A_a}. \tag{3.12}$$

As seen in equation (3.11), the sheath oscillates linearly around an average value, $\bar{s}_a$, with an amplitude of s_{0a}. Equations for sheath *b* are found in a similar way and are shown below in equations (3.13) - (3.15).

$$I_{bp}(t) = -\epsilon_0 n_i A_b \frac{d}{dt} s_a(t) \tag{3.13}$$

$$s_b(t) = \bar{s}_b + s_{0b} \sin(\omega t) \tag{3.14}$$

$$s_{0b} = \frac{I_1}{en_i \omega A_b} \tag{3.15}$$

The voltage across the sheath is found by integrating the electric field as shown in equation (3.8), and is given by

$$V_{ap}(t) = \int_0^{s_a(t)} E(x,t)dx = -\frac{en_i s_a^2(t)}{2\epsilon_0}. \tag{3.16}$$

Equation (3.16) shows that the voltage across the sheath is a non-linear function of the sheath size. Combining equation (3.11) and equation (3.16) yields,

$$\begin{aligned} V_{ap}(t) = -\frac{en_i}{2\epsilon_0}\Big[\bar{s}_a^2 + \frac{1}{2}s_{0a}^2 - 2\bar{s}_a s_{oa}\sin(\omega t) \\ -\frac{1}{2}s_{0a}^2\cos(2\omega t)\Big] \end{aligned} \tag{3.17}$$

which reveals that a sinusoidal current produces a sheath voltage that contains the second harmonic frequency as well as a DC offset value. The voltage developed across sheath *b* is found similarly and is shown in equation (3.18),

$$\begin{aligned} V_{bp}(t) = -\frac{en_i}{2\epsilon_0}\Big[\bar{s}_b^2 + \frac{1}{2}s_{0b}^2 + 2\bar{s}_b s_{ob}\sin(\omega t) \\ -\frac{1}{2}s_{0b}^2\cos(2\omega t)\Big]. \end{aligned} \tag{3.18}$$

For typical discharges, the voltage across the bulk plasma is much smaller than the voltage across both sheaths, $|\tilde{V}_p| \ll |\tilde{V}_{ab}|$, leading to the voltage across the entire discharge as the combination of sheath voltages $\tilde{V}_{rf} \approx \tilde{V}_{ab} = V_{ap} - V_{bp}$, and is shown in equation (3.19).

$$V_{rf}(t) \approx -\frac{en_i}{2\epsilon_0}\Big[\bar{s_a}^2 + \frac{1}{2}s_{0a}^2 - 2\bar{s_a}s_{0a}\sin(\omega t)$$

$$-\frac{1}{2}s_{0a}^2\cos(2\omega t) - \bar{s_b}^2 \tag{3.19}$$

$$-\frac{1}{2}s_{0b}^2 - 2\bar{s_b}s_{0b}\sin(\omega t) + \frac{1}{2}s_{0b}^2\cos(2\omega t)\Big]$$

For symmetric discharges, the discharge voltage reduces as follows;

$$A_a = A_b = A \tag{3.20}$$

$$s_a(t) = \bar{s} - s_0\sin(\omega t) \tag{3.21}$$

$$s_b(t) = \bar{s} + s_0\sin(\omega t) \tag{3.22}$$

$$s_o = \frac{I_1}{en_i\omega A} \tag{3.23}$$

$$V_{rf}(t) \approx V_{ab}(t) = \frac{2en_i\bar{s}s_0}{\epsilon_0}\sin(\omega t) \tag{3.24}$$

where $\bar{s}$ is the average sheath width and is constant. As seen in equation (3.24), a sinusoidal applied current results in a linear voltage in the symmetric discharge case. For asymmetrical sheath areas, $A_a \neq A_b$, the total voltage drop across the plasma, V_{ab}, remains non-linear with an applied linear current.

As stated earlier there is a small conduction current in addition to the displacement current through each of the sheaths. The conduction current is composed of a steady ion current, I_i, and an electron current, I_e, that only flows momentarily once per cycle. Given that there are no electrons within the sheath and by symmetry, the time average conduction current must be zero, the sheath width must collapse to zero in order for electrons to flow between the bulk plasma and the electrode. The collapse of the sheath width allows us to set the sheath width

amplitude and the time average sheath width to be equal, $s_0 = \bar{s}$, for each sheath. Applying this to the sheath width equation for sheath a, (3.11), and applying to the sheath width amplitude equation, (3.12), gives

$$s_a(t) = \frac{I_1}{en_i\omega A_a}[1 - \sin(\omega t)], \tag{3.25}$$

and a similar equation for sheath b

$$s_b(t) = \frac{I_1}{en_i\omega A_b}[1 + \sin(\omega t)]. \tag{3.26}$$

Applying the collapsing sheath width to the sheath voltage equations, (3.17)-(3.18), yields

$$V_{ap}(t) = -\frac{en_i}{2\epsilon_0}\left(\frac{I_1}{en_i\omega A_a}\right)^2 [1 - \sin(\omega t)]^2 \text{ and} \tag{3.27}$$

$$V_{bp}(t) = -\frac{en_i}{2\epsilon_0}\left(\frac{I_1}{en_i\omega A_b}\right)^2 [1 + \sin(\omega t)]^2. \tag{3.28}$$

Before continuing with the displacement current nonlinearity, we briefly discuss the conduction current. The electron current through the sheath behaves like an ideal diode. When the sheath width goes to zero, electrons from the bulk plasma are free to conduct to the electrode, thus creating an electron current from the electrode to the plasma. The amount of electron current that flows balances out the steady ion current such that the time average conduction current is zero. However, since the electron current is not sinusoidal in nature, it will still produces harmonics. Shown in Figure 2.3 (top) is a depiction of a sinusoidal voltage with a non-sinusoidal conduction current. The electron current is zero, except for around the time of sheath collapse. The resulting spikes of conduction current produce

harmonics as shown in the frequency spectrum of the current waveform, Figure 2.3 (bottom).

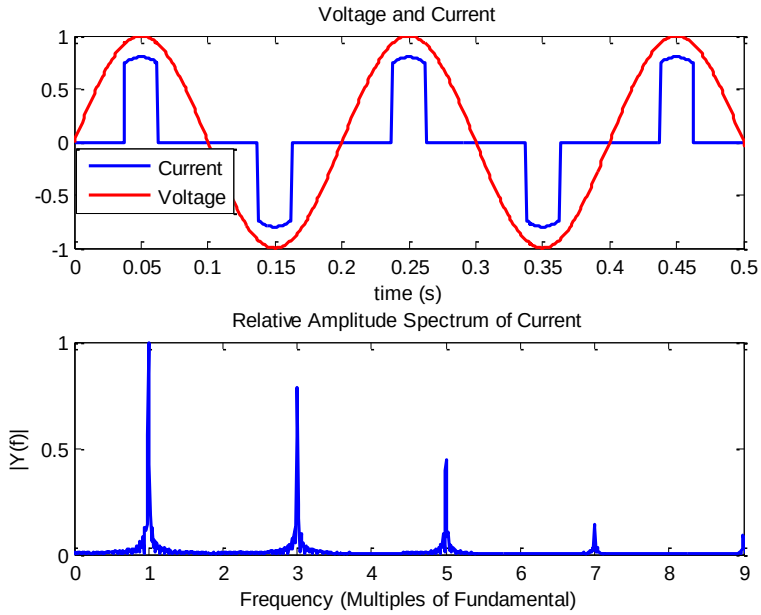

Figure 3.3. (Top) Time domain depiction of conduction current resulting from sheath collapse. (Bottom) Normalized frequency spectrum of conduction current

The above expressions for the voltage are now used to determine the values of the displacement currents through the sheaths. The capacitance of sheaths are found by modeling the sheaths as parallel plate capacitors using the equation

$$C = \frac{\epsilon_0 A}{d}. \tag{3.29}$$

Setting plate distance, *d*, to the time varying sheath width yields

$$C_a(t) = \frac{\epsilon_0 A_a}{s_a(t)} \text{ and} \tag{3.30}$$

$$C_b(t) = \frac{\epsilon_0 A_b}{s_b(t)}. \tag{3.31}$$

Inserting equations (3.25) and (3.26) into (3.30) and (3.31) gives the time dependent sheath capacitances

$$C_a(t) = \frac{\epsilon_0 A_a}{\frac{I_1}{en\omega A_a}[1 - \sin(\omega t)]} \text{ and} \tag{3.32}$$

$$C_b(t) = \frac{\epsilon_0 A_b}{\frac{I_1}{en\omega A_b}[1 + \sin(\omega t)]}. \tag{3.33}$$

Given that the sheaths are in series, the total sheath capacitance is expressed as the series combination of the two separate sheath capacitances and is expressed as

$$\begin{aligned} C_s(t) &= \left[\frac{1}{C_a(t)} + \frac{1}{C_b(t)}\right]^{-1} \\ &= \frac{A_a^2 A_b^2 e n_i \epsilon_0 \omega}{I_1[A_a^2 + A_b^2 + A_a^2 \sin(\omega t) - A_b^2 \sin(\omega t)]}. \end{aligned} \tag{3.34}$$

Equation (3.34) shows that the total capacitance across the plasma discharge is a function of the applied time-varying current and thus itself time-varying. In addition to the dependence on the time-varying current, the combined sheath capacitance is also dependent on the electrode areas A_a and A_b. When the electrode areas are symmetric ($A_a = A_b$) then the individual sheath capacitance nonlinearities cancel each other out to maintain a constant discharge capacitance. However, with asymmetric electrode areas ($A_a \neq A_b$) the resulting capacitance has a time-varying nature. These two scenarios are shown in Figure 3.4 for a microwave microplasma having discharge typical of conditions used for the experiments in section 7.

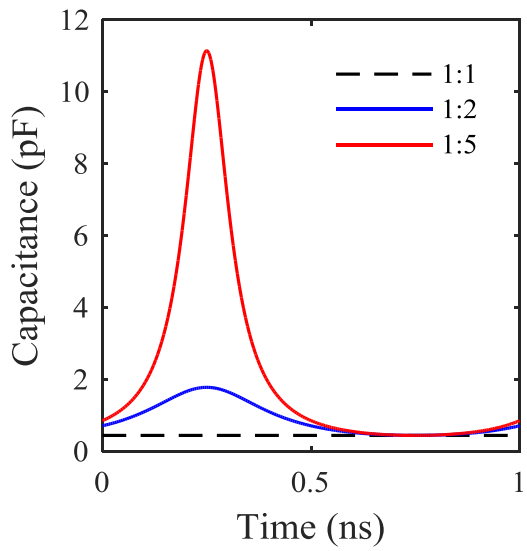

Figure 3.4. Total discharge capacitance (C_s) as a function of time during one period for a typical 1 GHz microwave microplasma discharge with electrode area ratios of 1:1 (black-dashed), 1:2 (blue-solid), and 1:5 (red-solid).

Using the above assumption of $s_0 = \bar{s}$ for both sheaths, we can simplify the voltage across both sheaths, (3.19), by introducing the simplifying variable *S*.

$$S = \frac{I_1}{en_i\omega} \tag{3.35}$$

Inserting the variable *S* into equations (3.12) and (3.15) results in

$$\bar{s_a} = s_{0a} = \frac{S}{A_a} \tag{3.36}$$

$$\bar{s_b} = s_{0b} = \frac{S}{A_b} \tag{3.37}$$

Inserting equations (3.36) and (3.37) into the voltage equation (3.19) yields

$$V_{rf}(t) \approx -\frac{en_i}{2\epsilon_0}\left[\frac{S^2}{A_a^2} + \frac{1}{2}\frac{S^2}{A_a^2} - 2\frac{S^2}{A_a^2}\sin(\omega t)\right.$$

$$-\frac{1}{2}\frac{S^2}{A_a^2}\cos(2\omega t) - \frac{S^2}{A_b^2} - \frac{1}{2}\frac{S^2}{A_b^2} - 2\frac{S^2}{A_b^2}\sin(\omega t)$$

$$\left.+\frac{1}{2}\frac{S^2}{A_b^2}\cos(2\omega t)\right] \tag{3.38}$$

Simplifying and re-arranging equation (3.38) yields

$$V_{rf}(t) \approx \frac{I_1^2}{4\epsilon_0 e n_i \omega^2}\left[3\left(\frac{1}{A_b^2} - \frac{1}{A_a^2}\right)\right.$$

$$+4\left(\frac{1}{A_b^2} + \frac{1}{A_a^2}\right)\sin(\omega t)$$

$$\left.+\left(\frac{1}{A_a^2} - \frac{1}{A_b^2}\right)\cos(2\omega t)\right] \tag{3.39}$$

With the voltage across the plasma in the form of equation (3.39), it is easy to see that for an asymmetric discharge there exist a DC bias, the fundamental frequency, and a second harmonic frequency. Each of the frequency components is a function of the electrode areas. I define a level of asymmetry as the ratio between the electrode areas,

$$Ratio = \frac{A_b}{A_a}. \tag{3.40}$$

The top left of Figure 3.5 depicts V_{rf}, equation (3.39), in graphical form for *Ratio* values of 1, 2, and 5. The remaining plots consist of frequency spectra at those same *Ratio* values. This figure clearly shows the non-linear nature of the voltage resulting from asymmetric discharge areas.

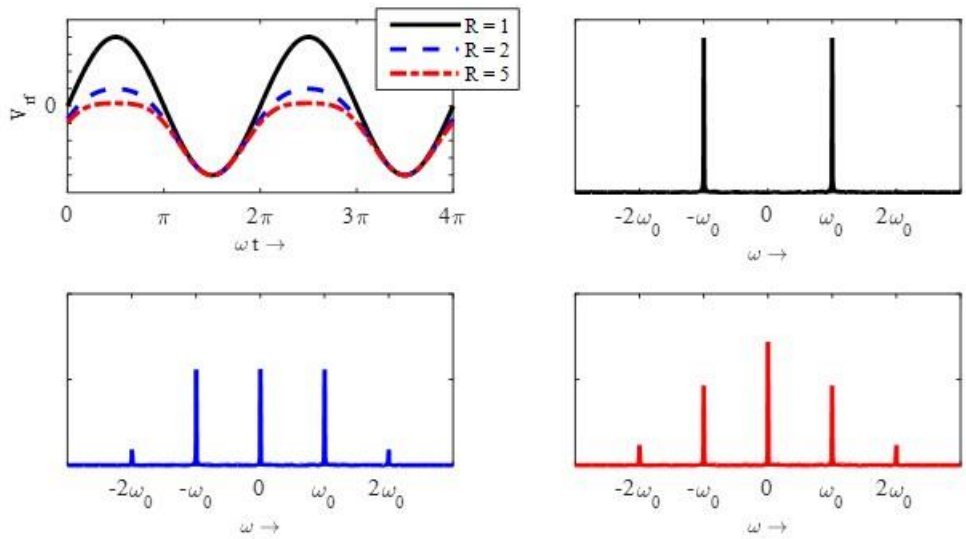

Figure 3.5. (Top Left) Normalized voltage across the plasma for varying discharge area ratios. Frequency spectrum of the voltage for a Ratio=1 (Top Right), Ratio=2 (Bottom Left), and Ratio=5 (Bottom Right)

A plot of the normalized amplitudes of each of the frequency components of the voltage is shown in Figure 3.6. It is apparent that with symmetric electrodes (*Ratio* = 1), only the fundamental frequency component remains within the voltage. However, once there is asymmetry in the electrode areas (*Ratio* > 1), the fundamental amplitude begins to decrease, while a negative DC offset and a positive second harmonic amplitude emerge. The frequency components asymptotically approach values of 37.5%, 50% and 12.5% of the symmetric fundamental amplitude for the DC, fundamental, and second harmonic frequencies respectively. As can be seen in Figure 3.6, the frequencies components reach their asymptotic values at a relatively modest area ratio.

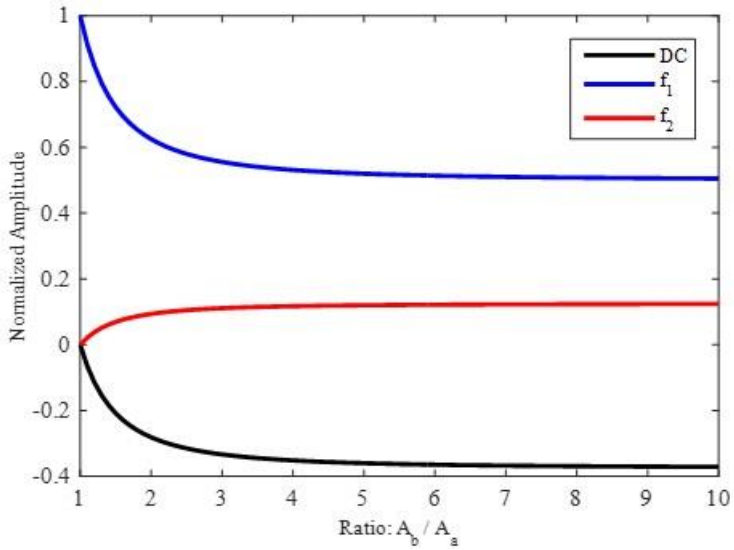

Figure 3.6. Normalized amplitudes of the DC, fundamental (f_1), and second harmonic (f_2) components of the voltage across the plasma as a function of the electrode area asymmetry ratio

3.4. Circuit Model

A simplified analysis of the plasma discharge can be accomplished by combining the previous analysis of the bulk plasma and sheaths into a circuit model. Figure 3.7 depicts the complete circuit model containing all the elements as discussed previously.

As was stated in section 3.2, the bulk plasma is represented by a vacuum capacitance, C_0, in parallel with the series combination of the plasma conductance, L_p, and a plasma resistance, R_p. These bulk plasma elements are placed in series between the two sheaths and is shown in Figure 3.7.

The sheaths are depicted in Figure 3.7 by parallel combinations of a current source, a diode, and a capacitance. The current sources, I_{ia} and I_{ib} represent the

constant, but small ion current within the sheaths. The diodes, D_a and D_b, allow an electron current to flow during the period when the sheaths collapse, representing the countering electron current. Finally, the capacitors, C_a and C_b, represent the non-linear capacitance developed by the time-varying sheath widths.

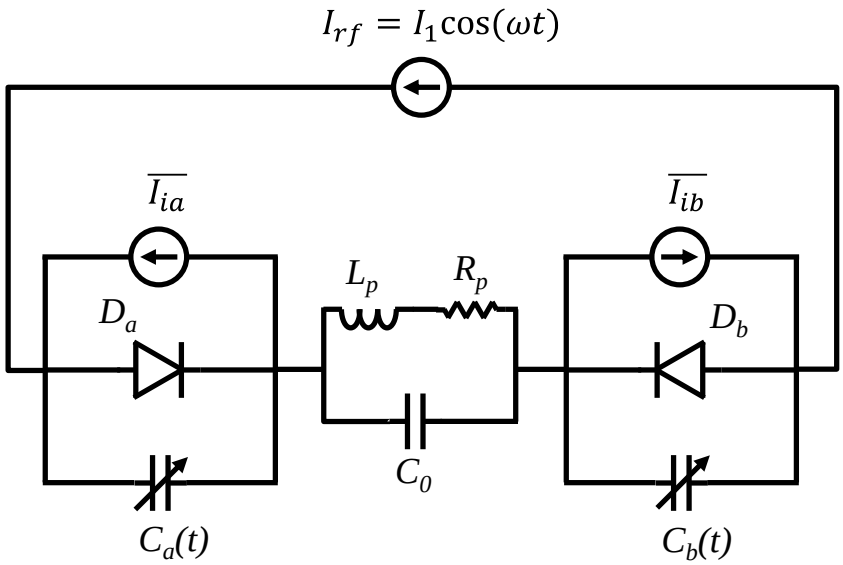

Figure 3.7. Circuit representation for simplified plasma matrix sheath model

The circuit model shows the similarities between a plasma and the semiconductor based harmonic multipliers from Section 2. The Schottky barrier diode multiplier relies on the non-linear nature of the diode element to produce harmonics. This same behavior occurs in the plasma sheath with the modulation of the conduction current. For HBV's, the nature of the depletion region, which causes a non-linear capacitive-voltage relationship, is analogous to the non-linear sheath capacitance of the time-varying sheath in the plasma. One of the biggest drawbacks of the semiconductor-based multipliers, low carrier mobility, is overcome with

plasmas due to the naturally high mobility of electron motion in low pressure gases. Additionally, the breakdown voltage of semiconductors hampers harmonic output due to the limitation of maximum input voltage. In plasmas, breakdown is the natural state, and as such, much higher voltages can be applied.

4. Properties of Microstrip Circuits

Microstrip circuits consist of a dielectric substrate with a thin layer of conducting material (typically copper) covering the entire bottom of the substrate to act as the ground plane and another thin layer of copper on the top of the dielectric in the shape of the desired circuit. Since the electric and magnetic fields propagate within the dielectric between the conducting circuit and the ground plane, as well as the region of air above the conducting circuit, microstrip circuits operate in a quasi-TEM mode [40].

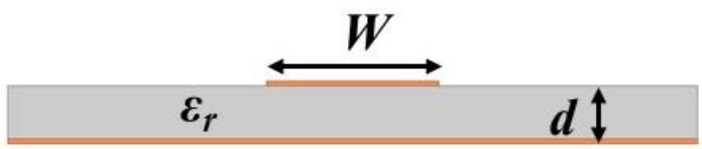

Figure 4.1. Microstrip side view configuration with a dielectric thickness of d, and conducting strip of width W

For a microstrip circuit as shown in Figure 4.1 with a conducting strip of width, W, a substrate thickness, d, and a relative dielectric constant of ε_r, an effective dielectric constant, ε_e, is given by equation (4.1).

$$\epsilon_e = \frac{\epsilon_r + 1}{2} + \frac{\epsilon_r - 1}{2} \cdot \frac{1}{\sqrt{1 + 12\, d/W}} \tag{4.1}$$

The effective dielectric, ε_e, replaces the dielectric constant, ε_r, for all equations relating to the microstrip structure, such as wavelength and characteristic impedance as shown in equations (4.2) and, (4.3) where, λ, is the wavelength within the copper conductor, f, is the operating frequency and c, is the speed of light [40].

$$\lambda = \frac{c}{f\sqrt{\epsilon_e}} \tag{4.2}$$

$$Z_0 = \begin{cases} \frac{60}{\sqrt{\epsilon_e}} \ln\left(\frac{8d}{W} + \frac{W}{4d}\right), & W/d \leq 1 \\ \frac{120\pi}{\sqrt{\epsilon_e}\left[\frac{W}{d} + 1.393 + 0.667 ln\left(\frac{W}{d} + 1.444\right)\right]}, & W/d \geq 1 \end{cases} \tag{4.3}$$

5. Microstrip Split Ring Resonator Plasma Source

In order to examine harmonic generation via plasma, I designed a microstrip split ring resonator (SRR) plasma source similar to ones first developed by Iza and Hopwood [9]. The MSRR design allows for operation at a wide array of power levels and pressures, which is ideal for the desired experiments. In order to investigate the effect of electrode area asymmetry on harmonic generation, a plasma limiter consisting of a block of dielectric material with a 180° cutout was added to the SSR device. The plasma limiter is rotated to allow for device operation with various electrode areas exposed to the plasma.

5.1. Microstrip Split Ring Design

The microplasma source consist of a split ring resonator (SRR) on a microwave substrate, as shown in Figure 1, and first described in [9]. The microwave substrate consists of 60 mils (1.5 mm) thick Rogers TMM® 10 ($\varepsilon_r = 9.2$) with 35 μm thick copper plating on both the top and bottom sides. Using a LPKF Protomat S60, copper from the top surface of the substrate is removed to form a 1 mm wide split ring with a center radius of 8.0 mm. The split ring has a discharge gap of 150 um and has tapered points to increase the electric field for easier starting of the plasma. A 1 mm wide copper strip from the split ring to the substrate edge allows the center conductor of an SMA connector to be soldered to the input line of the split ring while the ground of the connector is soldered to the ground plane of the microstrip. The split ring gap is rotated around the center axis by 12° in order to match the impedance of the split ring to the 50 Ω microwave source [11]. A schematic of the SRR design is shown in Figure 5.1.

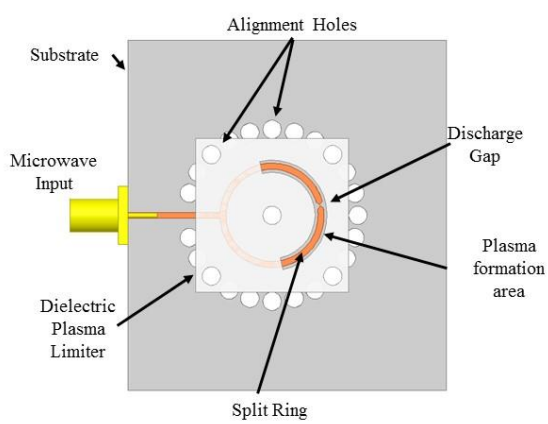

Figure 5.1. Single Microstrip Split Ring Resonator with SMA connection

To create electrode asymmetry, a dielectric plasma limiter is placed on top of the split ring. The plasma limiter is constructed of a block of 20 mm thick Macor® with a 180° semicircular cutout. The limiter prevents plasma formation where it is in contact with the split ring. The thickness of the dielectric limiter allows the plasma to expand upwards during high power operation without expanding onto the substrate.

Rotating the limiter around the center axis of the SRR allows the cutout to expose varying areas of the electrodes to be exposed. Alignment holes drilled into the limiter and the microstrip substrate allow the ratio of the electrode areas to be consistent between rotations of the limiter. Electrode area ratios of 1:1, 3:1, and 110:1 is achieved by rotating the limiter counter-clockwise by 0°, 45°, and 90° respectively, as seen in Figure 5.2. It is important to note that at low pressures, the plasma is able to diffuse to fill the plasma limiter cutout. At higher pressures, the plasma localizes around the gap region [41] and the dielectric limiter has little to no effect.

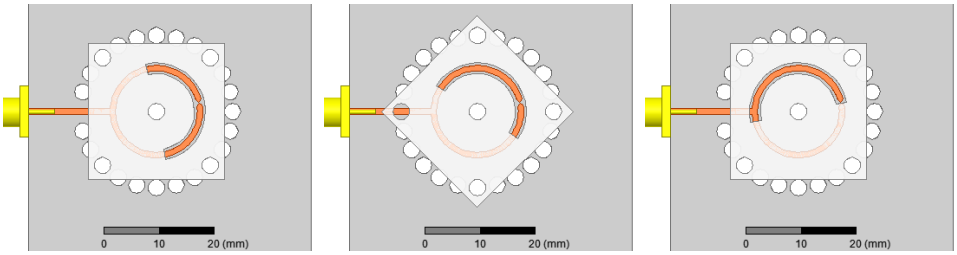

Figure 5.2. Dielectric plasma limiter positions: (Left) 0°, (Center) 45° CCW, (Right) 90° CCW.

When the resonant frequency is applied to the resonator, a standing wave will develop with voltage peaks at each end, but with opposite polarity. A standing current waveform is also developed, with the current peak at the center of the resonator length and the current going to zero at the gap. This is illustrated in Figure 5.3. This large voltage difference across the small gap creates a strong electric field that under the right environmental conditions, ignites a plasma.

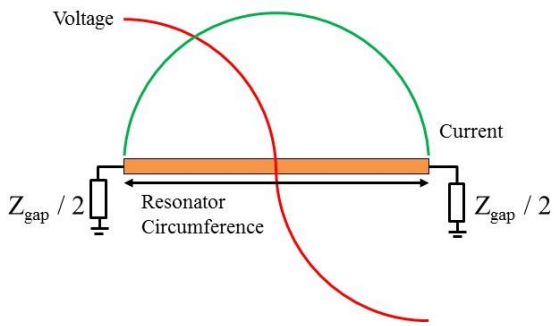

Figure 5.3. Voltage and current standing wave patterns for a half-wave resonator

A resonant frequency of 1.212 GHZ is calculated by means of equation (4.2) where the wavelength, λ, is one-half of the circumference (50.3 mm) of the split ring. This approximant resonant frequency was chosen to accommodate the measurement of both the fundamental frequency and the reflected third harmonic frequency using a single broadband 1 GHz to 4 GHz directional coupler. The experimental setup is described further in section 6. A summary of the design parameters is found in Table 1.

Table 1. SRR design parameters

Parameter	**Value**
Substrate	Rogers TMM® 10
Thickness	60 mils (1.524 mm)
Dielectric Constant (ε_r)	9.2
SRR Center Radius	8.0 mm
Discharge Gap	150 μm
Calculated Characteristic Impedance	61.3 Ω
Calculated Resonant Frequency	1.212 GHz

5.2. Simulation Results

Using the design parameters as shown in Table 1, the SRR was simulated using Ansys® High Frequency Structural Simulator (HFSS™). HFSS is a 3-D electromagnetic simulator utilizing the finite element method to numerically solve Maxwell's equations.

Using HFSS, the resonant frequency of the SRR can be found by observing the simulated reflection coefficient (S_{11}). The resonant frequency occurs when the reflection coefficient shows a steep minimum as seen in Figure 5.4 for SRR without the dielectric plasma limiter. Here the resonant frequency is simulated to be 1.221 GHz.

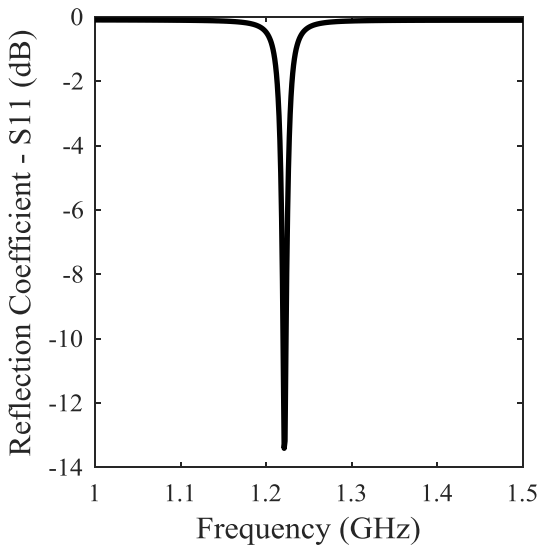

Figure 5.4. Simulated reflection coefficient (S_{11}) of the SRR without the dielectric plasma limiter

The simulated resonant frequency of 1.221 GHz is 9 MHz higher than from the calculated resonant frequency of 1.212 GHz for several reasons. Firstly, the calculated resonant frequency did not take into account the discharge gap capacitance. The gap capacitance has the effect of making the electrical path longer, which increases the half-wavelength, which leads to a slightly lower resonant frequency. Secondly, the gap width was not subtracted from the half-wavelength (ring circumference) used in the calculation. With a shorter half-wavelength, the resonant frequency will be slightly higher. Lastly, the taper applied to each side of the discharge gap as the effect of shortening the effective current path around the ring. This shorter path reduces the half-wavelength, which in turn increases the resonant frequency of the SRR. These three effects lead to an overall increase in the resonant frequency.

As discussed earlier and as shown in Figure 5.3, a voltage standing wave pattern develops along the resonator when excited with the resonant frequency; this is seen in Figure 5.5. Shown is the complex amplitude of the electric field along the split ring with the discharge gap enlarged for clarity. The electric field is largest at the tips of the electrodes with a weak electric field along the length of the ring. This is analogous to the voltage standing wave pattern expected of a half-wave resonator.

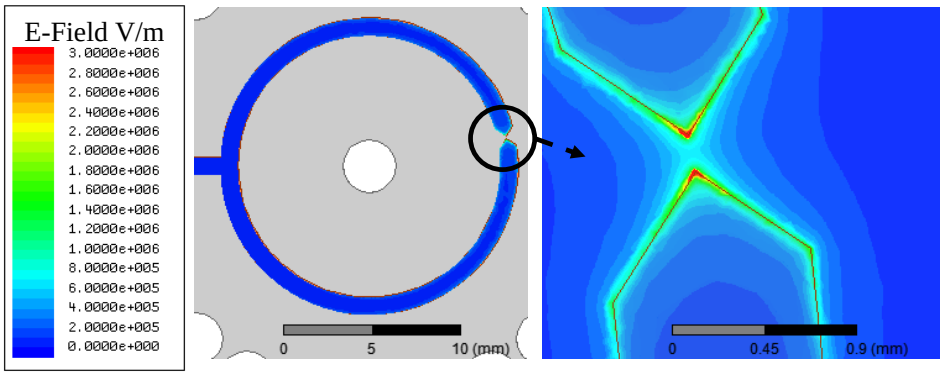

Figure 5.5. HFSS simulation showing the complex electric field magnitude of the MSRR with a zoomed in picture of the gap (1 W forward power; Maximum e-field $3x10^6$ V/m)

In addition to a voltage standing wave, a current standing wave also appears along the SRR when the resonant frequency is applied. Shown in Figure 5.6 is the simulated surface current density along the SRR. The current density peaks opposite to the discharge gap and decreases along the split ring to zero current density at the gap itself. This is analogous to the current standing wave shown in Figure 5.3.

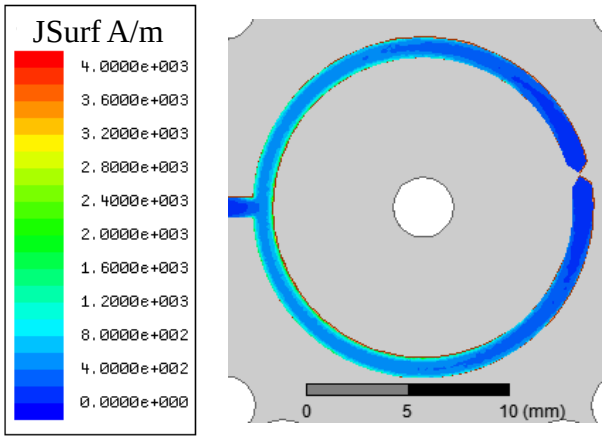

Figure 5.6. HFSS simulation showing current density of the SRR

The addition of the dielectric plasma limiter to the SRR will limit the plasma formation area, but as a consequence, the electric fields above the SRR are also effected. This modification of the electric fields modifies the effective dielectric constant (ε_e), which in turn modifies the resonant frequency of the SRR. This effect is highly complex and not readily calculated, and as such was not attempted. However, this effect is easily simulated using HFSS®. Using HFSS® a block of Macor® was added to the simulated and was run using three different rotations of the limiter; 0°, 45°, and 90°. These positions are shown in Figure 5.2. The resulting reflection coefficients (S11) are shown in Figure 5.7, along with the previous results without the dielectric limiter.

The simulation shows that the resonant frequency of the SRR is not only sensitive to the addition of the dielectric block, but the rotational position of the block as well. As seen in Figure 5.7, the addition of the dielectric limiter at the 0° (ratio 1:1) position reduces the resonant frequency from 1.221 GHz to 1.159 GHz.

This reduction in resonant frequency corresponds to an increase in ε_e, which is due to the high dielectric constant (ε_r) of the Macor® block replacing that of air. Rotating the dielectric limiter also shifts the resonant frequency of the SRR, but to a lesser extent. Resonant frequencies of 1.167 GHz and 1.141 GHz are realized for dielectric limiter position of 45° and 90° respectfully.

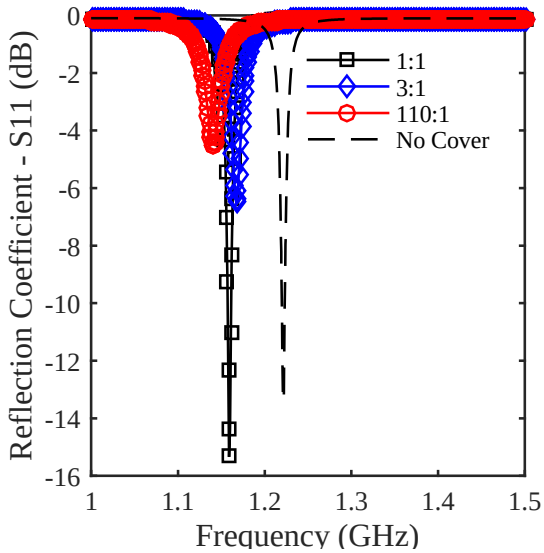

Figure 5.7. Simulated reflection coefficient (S_{11}) of the SRR with the dielectric plasma limiter at positions of 0°, 45°, and 90° CCW corresponding to electrode area rations of 1:1, 3:1, and 110:1 respectfully. Simulated results without the cover is also shown for reference.

6. Experimental Setup

Measurement of harmonic power is accomplished in two separate ways. First, to confirm the existence of harmonics, a broadband antenna collects radiated power from the split ring device. Second, with a plasma present, the impedance mismatch caused by the existence of the plasma results in a significant amount of reflected power. The reflected power contains not only the fundamental frequency but the

harmonics created by the plasma as well. A spectrum analyzer measures the frequency content in both cases. The general experimental setup is shown in Figure 6.1 with a dashed line showing the connections for radiation measurements and solid lines for the reflected power measurements.

The device is placed into a vacuum chamber and attached to a coaxial feedthrough. The feedthrough is attached to a broadband (1 to 4 GHz) directional coupler, which samples both the forward and reflected power for measurement. A microwave powertrain, consisting of signal generator and amplifier is connected to the directional coupler to feed the power at the fundamental frequency to the SRR.

Forward power to the SRR is measured using a power meter and power sensor that is connected to the forward power coupling port from the directional coupler and corrected for losses from the coupler to the device. Reflected power is measured in one of two ways depending on the experiment. For measurements involving the reflected power harmonics, a spectrum analyzer is attached to the reflected power port of the directional coupler with an inline high pass filter. The filter reduces the power of the reflected fundamental frequency in order to measure both the fundamental and harmonics simultaneously with the greatest accuracy. Without the filter, the third harmonic power may be lower than the noise level of the spectrum analyzer due to the high reference level needed to measure an unfiltered fundamental. The frequency spectrum of the reflected power is then corrected for cable loss, coupling loss, and loss from the filter for in the final measurement of the reflected power at all frequencies. As the harmonics are

quantified at the reflected port of the directional coupler, this measurement will be referred to as the reflected measurement method.

To measure the radiated power spectrum, a 1 to 18 GHz broadband antenna is connected to the spectrum analyzer through a high pass filter. The antenna is placed in front of the glass window in the vacuum chamber wall directly in-line with the SRR face. Forward power measured in the same manner as the reflected power measurement. Reflected power is measured using a second power meter connected to the reflected power port of the direction coupler and is corrected for cable and coupling losses. To correct the measured radiated power spectrum requires the radiation efficiency for each position of the plasma limiter and for each measured frequency, as well as propagation losses and corrections for the antenna. For these reasons, radiated measurements were made solely to show the existence of harmonics created by the plasma and to confirm the general trends shown by the reflected measurements.

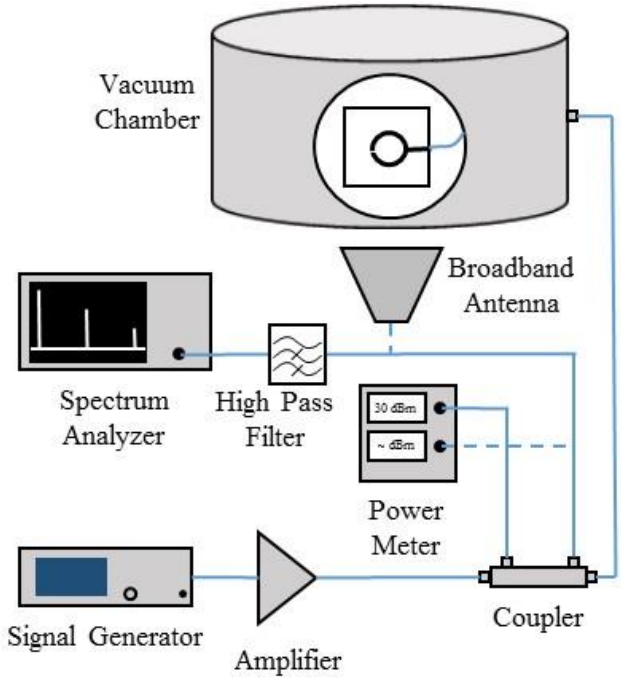

Figure 6.1. Experimental setup for measuring power spectrum reflected from the device. Dashed lines represent connections for radiated power measurements

7. Experimental Results

Harmonic power generated by plasma is affected by many different variables, in the following experiments three of these variable will be explored, input power, gas pressure, and electrode area asymmetry. A frequency sweep of the split ring device without the presence of a plasma was first conducted in order to characterize the harmonic content of the microwave powertrain. Using the reflected measurement experimental setup as shown in Figure 6.1, fundamental power was applied to the device and swept in frequency from 1-1.3 GHz. Third harmonic power was measured using the spectrum analyzer and corrected. This measurement was conducted in atmospheric pressure air to prevent ignition of a plasma. This

experiment was then repeated in 0.3 Torr of argon with a plasma present within the discharge gap of the device. The results of these two frequency sweeps is shown in Figure 7.1. This data shows that with the plasma present, third harmonic power is increased by a factor of ~1000 within the operating band of the device as compared to the third harmonic created by the microwave powertrain only.

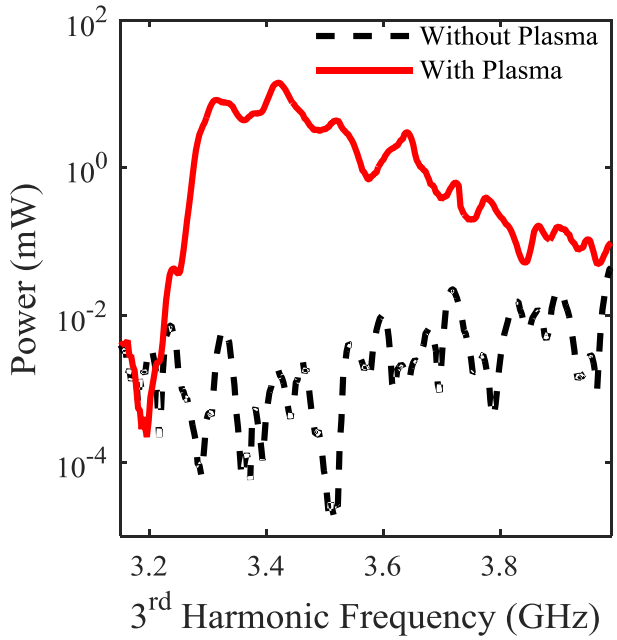

Figure 7.1. Third harmonic power from the amplifier reflected from the device without plasma (dashed black) and with plasma (solid red) in the fundamental frequency band of operation. Data with plasma was taken while in 0.3 Torr of argon and a constant forward power level of 3 W for both.

Using the broadband antenna, radiation from the SRR was measured at a single fundamental frequency in order to conduct a survey of harmonics created by both the microwave powertrain and of the plasma. A comparison of created harmonics is shown in Figure 7.2. Without a plasma present, the microwave powertrain

radiates harmonics up to and including the fourth harmonic before disappearing below the noise floor of the spectrum analyzer. With a plasma present in 0.3 Torr Argon, the radiation from the SRR contains the applied fundamental frequency as well as both odd and even harmonics out to the 7th harmonic. Additional harmonics could not be measured due to the noise floor of the spectrum analyzer.

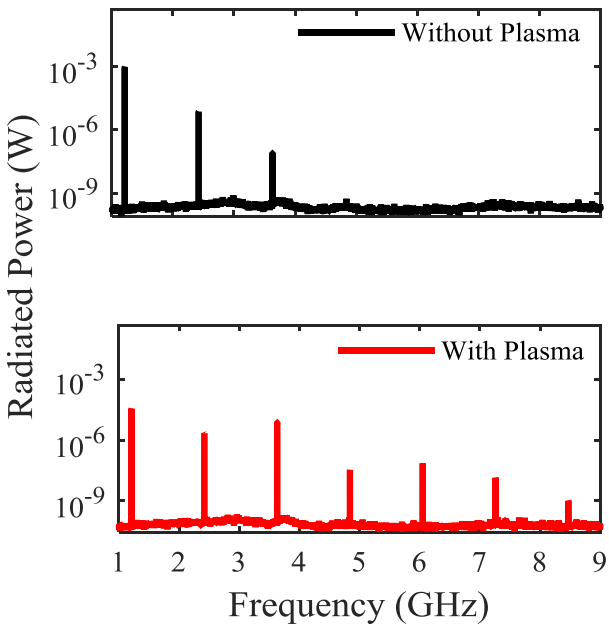

Figure 7.2. Measured radiated power from split ring resonator without plasma present (Top) and plasma present (Bottom). Measured Data was taken with SRR inside vacuum chamber with 0.3 Torr of Argon and 4 Watts of net power absorbed by microplasma.

To determine the effect of gas pressure on harmonic generation, a pressure sweep is conducted using the reflected power measurement setup. To determine the ideal frequency for which to conduct the pressure sweep, a frequency sweep is

conducted at each electrode asymmetry and the frequency at which the peak third harmonic power is generated is found.

For each asymmetry value, the pressure was swept at various values from 200 mTorr to 50 Torr at the pre-determined frequency. A constant forward power of 3.3 W was maintained throughout the experiment. These measurements were repeated for electrode asymmetry ratios of 1, 3, and 110. All measurements where corrected for cable and coupling losses.

The resulting third harmonic power measurements are plotted in Figure 7.3. Third harmonic power is shown to be dependent on both gas pressure and electrode area asymmetry. At all pressures, third harmonic power is increased with asymmetry but appears to asymptotically approach a maximum value. For asymmetry ratios of 1:1 and 3:1, third harmonic power decreases rapidly from the peak value at 300 mTorr for both an increase and decrease in gas pressure. For the 110:1 ratio, third harmonic power follows a similar pattern for pressures higher than 300 mTorr. For pressures below 300 mTorr, the third harmonic power remains relatively steady, however, pressures below 200 mTorr were not measured due to limitations in the vacuum chamber equipment. At low pressures (below ~10 Torr), the plasma is diffuse and fills the cutout in the dielectric plasma limiter, however, at higher pressures; the plasma condenses around the gap and begins to loose asymmetry. This accounts for the rapid decrease in harmonic generation for the 110:1 and 3:1 ratios as compared to the 1:1 ratio.

Due to plasma impedance dependence on gas pressure, the frequency at which the third harmonic power will be maximum can vary. For this reason, third

harmonic power was measured for the 110:1 electrode area ratio at pressures ranging from 200 mTorr to 750 Torr while sweeping the full frequency range. The inset for Figure 7.3 shows a comparison between recording the harmonic power at a single frequency (shown in red with circle markers) and recording the maximum harmonic power regardless of frequency (shown in green with star markers). This comparison shows that at around 10 Torr a significant impedance change occurs that shifts the peak harmonic output in frequency.

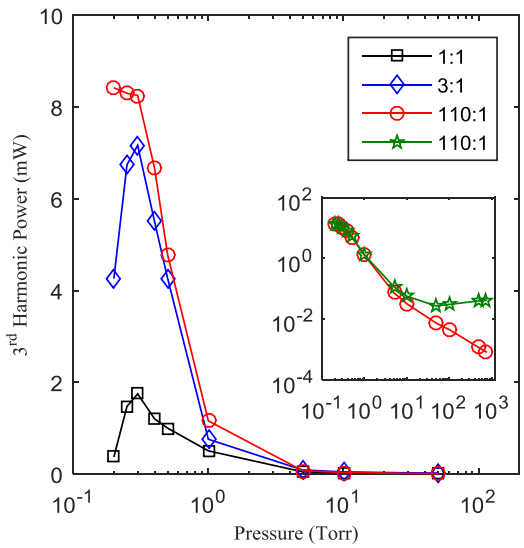

Figure 7.3. Measured reflected power of the third harmonic versus pressure for various electrode asymmetry ratios. All data taken in Argon with a constant forward power of 3.3 W. (Inset) A comparison between single frequency measurement and the max power level at each pressure regardless of frequency.

Based on the pressure sweep data shown in Figure 7.3, a gas pressure of 0.3 Torr was chosen to conduct a power sweep. For each electrode area ratio, fundamental input power was applied to the device while measuring the amount of reflected power. Net power was calculated by subtracting the amount of reflected

power from the forward applied power after all corrections were applied. Input power was swept while collecting third harmonic power reflected from the device using a spectrum analyzer.

The third harmonic power produced by the plasma has a strong dependence on the fundamental input power as shown in Figure 7.4. As was shown in the pressure sweep data, the power sweep also shows that third harmonic output is also dependent on electrode area asymmetry.

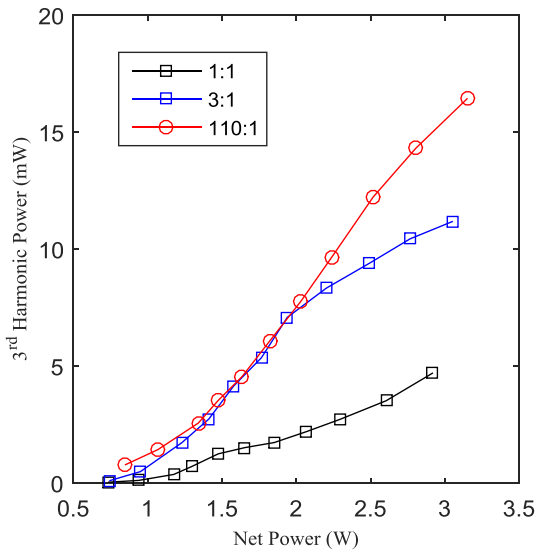

Figure 7.4. Measured reflected third harmonic power versus net absorbed power by the microplasma for various electrode asymmetry ratios. Data taken in Argon at 0.3 Torr.

Using the broadband antenna, radiation measurements of the third harmonic power can be compared to that of the reflection measurements. A comparison of the reflected and radiated measurements for the 1:1 and 110:1 electrode area ratios is seen in Figure 7.5. Data was taken in 0.5 Torr of Argon and swept in input power.

As before, the radiation data is not corrected for any losses due to the complexity, but it shown here on a separate axis to compare the general trends in third harmonic power generation. The figure shows consistent trends for both measurements methods. Third harmonic power increases similarly for both radiated and reflected data. Measured radiated power is a scaled version of reflected power.

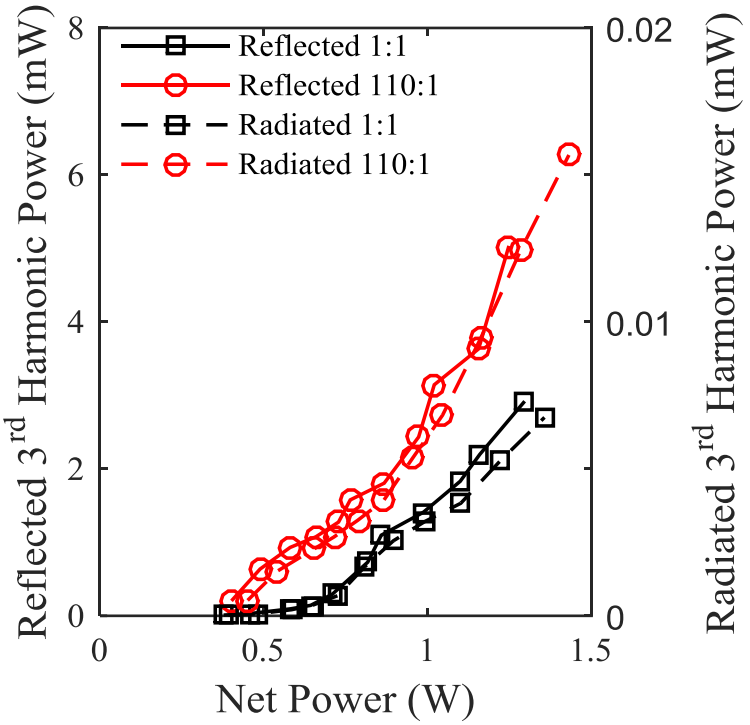

Figure 7.5. Measured reflected and radiated power of the third harmonic power versus net power to the device. Data was taken in Argon at 0.5 Torr.

The same non-linear voltage-current relationship used for harmonic generation can also be exploited for frequency mixing. Frequency mixers utilize two separate input frequencies (f_1 and f_2) to generate a sum frequency ($f_1 + f_2$) and a difference frequency ($f_1 - f_2$). Depending on the type of mixer desired, up-conversion (sum), or

down-conversion (difference) the output is filtered to delivery only the appropriate frequency.

Starting with the same microwave circuit as shown in Figure 1, adding 50 Ω input and output lines perpendicular to the discharge electrodes will create a mixing device, Figure 7.6. In this configuration, the SRR is used to create and maintain the plasma, while a separate input signal is applied to the plasma via the 50 Ω input line. The input signal frequency is mixed with the frequency of the signal used to maintain the plasma. The mixed signal is output via the 50 Ω output line which is in direct contact with the plasma. This method of power extraction is inefficient, however, it is an easily implementable configuration to observe the production of mixing frequencies.

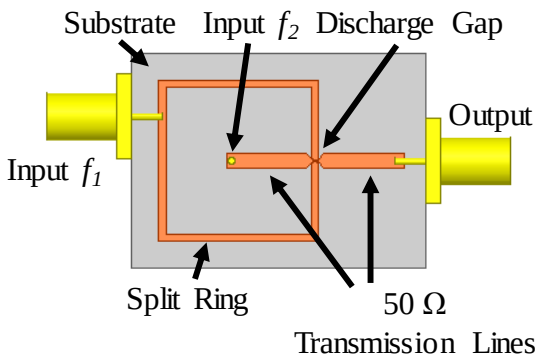

Figure 7.6. Plasma based frequency mixer configuration

For this experiment, a 1.05 GHz is applied to the input (f_1) to ignite and maintain the plasma. A separate signal of 1.0 GHz is applied to the second input (f_2) to create the requisite mixing effects. The two input signals are mixed within

the plasma at the discharge gap and the resulting power spectrum is sampled using a spectrum analyzer via the output transmission line.

The resulting power spectrum is shown in Figure 7.7. With only the 1.05 GHz input signal applied (f_1), the resulting power spectrum contains the fundamental frequency (1.05 GHz) and the second, third, and fourth harmonics as shown in the top left. Applying the second input (f_2) of 1.0 GHz results in the power spectrum shown in the top right. For this frequency mixing case, the sum frequency (2.05 GHz), the difference frequency (50 MHz), and both input frequencies are observed. In addition to the predicted mixing frequencies, intermodulation frequencies are also observed with a spacing of 50 MHz. The intermodulation frequencies are the result of mixing of the original mixing products. The mixing effect occurs for each new set of frequencies produced until the resulting output power spectrum contains power spaced every 50 MHz (the difference frequency). Shown in the bottom left of the figure is the resulting down-conversion power spectra, which clearly shows the difference frequency of 50 MHz, as well as intermodulation frequencies at 100, 150, 200, and 250 MHz. Beyond 250 MHz the intermodulation frequencies are below the noise floor of the spectrum analyzer and thus are not shown. The bottom left of the figure shows the up-conversion spectra, which includes the sum frequency (2.05 GHz) and intermodulation frequencies with 50 MHz spacing both above and below the sum frequency. Again, additional intermodulation frequencies are below the noise floor of the spectrum analyzer and are not shown.

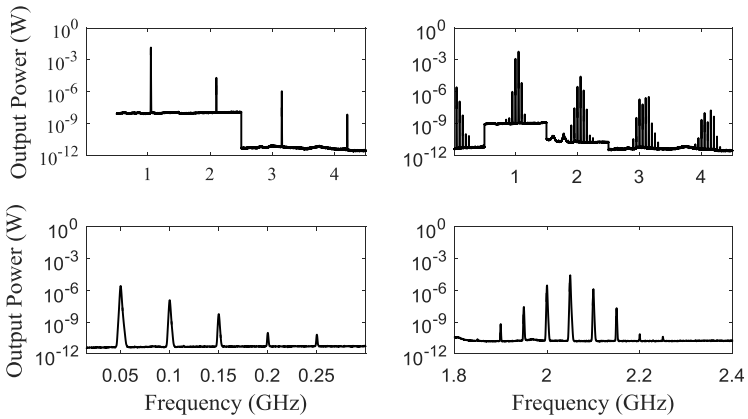

Figure 7.7. Output power spectra of mixer configuration. (Top Left) Single input frequency (f_1 = 1.05 GHz) with sustained plasma. (Top Right) Two input signals (f_1 = 1.05 GHz, f_2 = 1.0 GHz) with sustained plasma. (Bottom Left) Resulting down-conversion power spectra. (Bottom Right) Resulting up-conversion power spectra.

8. Fluid Model

Experimental results of harmonic creation by plasmas are not sufficient to understand the origins of the plasma nonlinearities. While a first order theoretical examination of plasma nonlinearity is shown in Section 3, a self-consistent numerical fluid model was separately developed by Gregorio [42] to help understand the relevant phenomena.

8.1. Fluid Model Description

The fluid model, which is a 2-D extension of the model reported in [43] and is further described in [42], solves the continuity and momentum equations for all species, as well as the energy and Poisson's equations. An electrostatic approximation is utilized due to the wavelength being much shorter that he plasma

characteristic dimensions. Additional approximations as well as a more complete description of the fluid model can be found in [42].

Modeling of the SRR is accomplished by creating the geometry as shown in Figure 8.1. Asymmetry is simulated by creating two electrodes with dissimilar lengths with the discharge gap between them. Plasma is allowed to form in the area above the electrodes (shown in white) with the dielectric material (shown in gray) preventing plasma formation. This plasma formation area is analogous to the dielectric plasma limiter from the experimental setup.

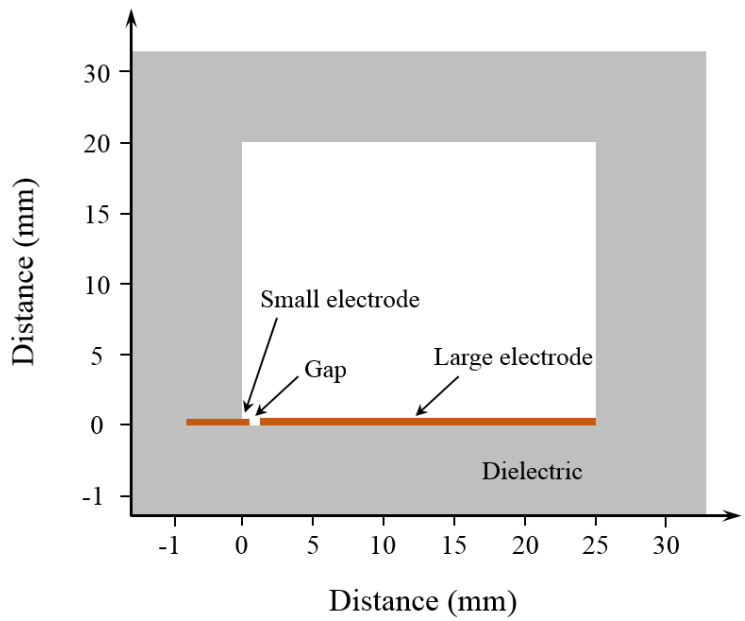

Figure 8.1. SRR geometry for fluid model, shown for fully asymmetric case (110:1 electrode area ratio) [42]

The model is given parameters of gas pressure and type, net power absorbed by the plasma, excitation frequency, and geometric sizes. A sinusoidal voltage that corresponds to a specified net power is applied to the short electrode while the long

electrode is grounded. Values of these parameters are the same as in the previous experiments. Values of plasma current and impedance are extracted from the model after a self-consistent solution to all equations is found.

8.2. Fluid Model Simulation Results

In this section I will summarize the results of the simulations using the model of Gregorio as reported in [42], and these results will then be compared to the experimental results later in section 8.3. The simulations results will mirror those from the experimental results for ease of comparison. First, the net power to the plasma is kept constant as the gas pressure is varied in order to find the optimum pressure for harmonic production. Second, the effects of absorbed power to the plasma is explored by varying the net power applied to the plasma while keeping a constant gas pressure. Both symmetric and asymmetric electrode configurations are explored, but the results are focused around the asymmetric case since it is clear from the experimental results that asymmetric electrodes produce significantly higher levels harmonic power.

In contrast to the circuit model discussed in section 3.4, the fluid model uses a sinusoidal voltage as the source instead of current, and as such, the non-linear behavior will be observed in the discharge current. Figure 8.2 shows the time evolution of the displacement, electron, and total current at the surface of the small electrode for an asymmetric configuration. At low pressures, a significant amount of electron current (blue lines) exist due to the high electron temperature and voltages accelerating electrons through the sheath. In addition, the displacement current (red lines) is deformed due to the non-linear nature of the sheath motion

(non-linear capacitance). These two effects combine to create a significant deformation from sinusoidal in the total current (black lines), which introduces harmonics. At 760 Torr, only small amounts of electrons are able to reach the electrode, and occurs only when the sheath potential is at a minimum. Furthermore, the displacement current through the sheath is now sinusoidal in nature due to the loss of the asymmetry at high pressure. The result is a near sinusoidal total current, which produces little to no harmonics.

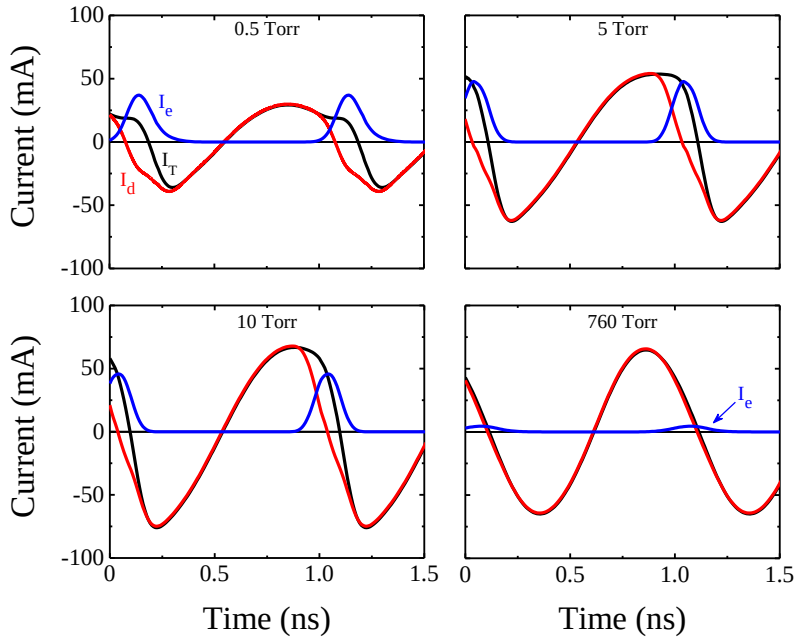

Figure 8.2. Temporal current waveforms for various gas pressures. Total current (I_T black), displacement current (I_d red) and electron current (I_e blue) are shown to the surface of the small electrode. [42]

To see the total effect of gas pressure on harmonic generation, the harmonic amplitudes were extracted from the total current (I_T) using the Fast Fourier Transform (FFT). The resulting current amplitudes as a function of gas pressure is

presented in Figure 8.3. As predicted by the preceding analysis, peak harmonic current is obtained at low pressure, however, below 10 Torr there is a significant drop in fundamental current, and therefore, 3rd harmonic current peaks at 10 Torr instead of lower as would be expected from the experimental results.

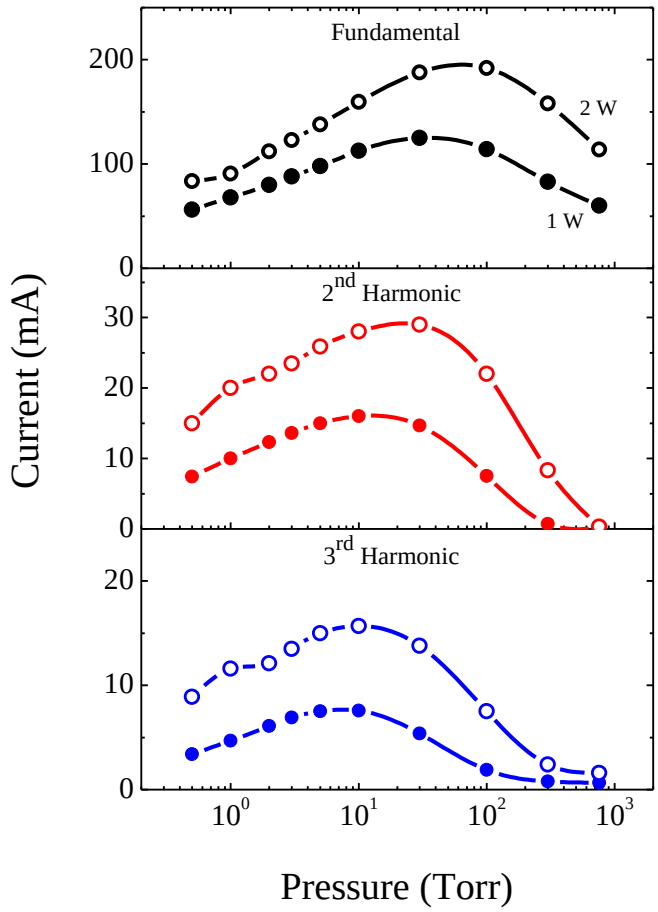

Figure 8.3. Current amplitudes of the fundamental, 2nd, and 3rd harmonics as a function of pressure for a constant 1 W (solid symbols) and 2 W (open symbols) absorbed power. [42]

Figure 8.3 also shows the effect of absorbed power on the harmonic current amplitudes, with 1 W and 2 W data displayed. To explore this further, the

simulation was run at 10 Torr, pressure at peak 3rd harmonic generation, for absorbed power levels of 0.5 W to 4 W. Figure 8.4 displays the results of this power sweep. With increasing power, the plasma discharge exhibits an increase in both total current (Figure 8.3) and applied voltage [42] which leads to a greater contribution of the electron current to the total current (not shown). This increased contribution further deforms the total current waveform, which increases harmonic current amplitudes. While the fundamental current doubles from a net power increase of 1 W to 4 W, the 3rd harmonic current triples during the same power increase, which shows that the 3rd harmonic increases at a faster rate than fundamental current.

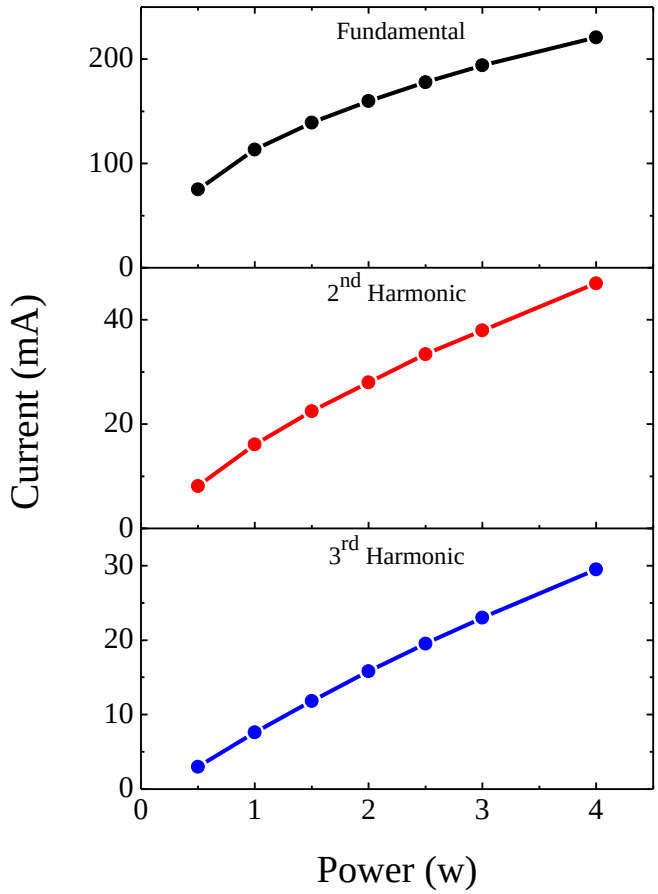

Figure 8.4. Current amplitudes of the fundamental, 2nd, and 3rd harmonics as a function of absorbed power to the plasma. [42]

8.3. Comparison with Fluid model

In order to compare the modeled results with the experimental power results, a circuit model was developed to convert the third harmonic plasma current and impedance into power. Since the experimental power measurements were taken, and corrected, as seen immediately leaving the SRR, the plasma current and impedance are not sufficient to directly calculate a comparable power reading. To

accomplish this, we use Agilent's Advanced Design System (ADS) to solve the circuit and transmission line equations to obtain the third harmonic power as seen from the exit of the SRR.

A schematic of the circuit model is shown in Figure 8.5 and consist of three main groups: (1) Measurement Circuit, (2) Microstrip SRR, and (3) Plasma Current and Impedance.

The Measurement Circuit section accounts for the measurement setup from the experimental setup as described earlier. The addition of the coupler and coaxial cables is important to capture the effect of standing waves due to any impedance mismatches caused by the SRR and the plasma. Three 50 Ω resisters are utilized in place of output impedance (50 Ω) of the power amplifier, forward power sensor, and spectrum analyzer used in the experimental setup. For this model, the power amplifier is assumed to only produce power at the fundamental frequency as such is nulled as this model only simulates the third harmonic frequency. In the experimental setup, the third harmonic power is measured using a spectrum analyzer attached to the reflected port of the coupler, and then corrected for coupling and cable losses to achieve power readings as would be seen at the input to the SRR. This is not required in ADS as a power measurement device can be placed anywhere within the circuit, and thus is placed at the input port to the SRR.

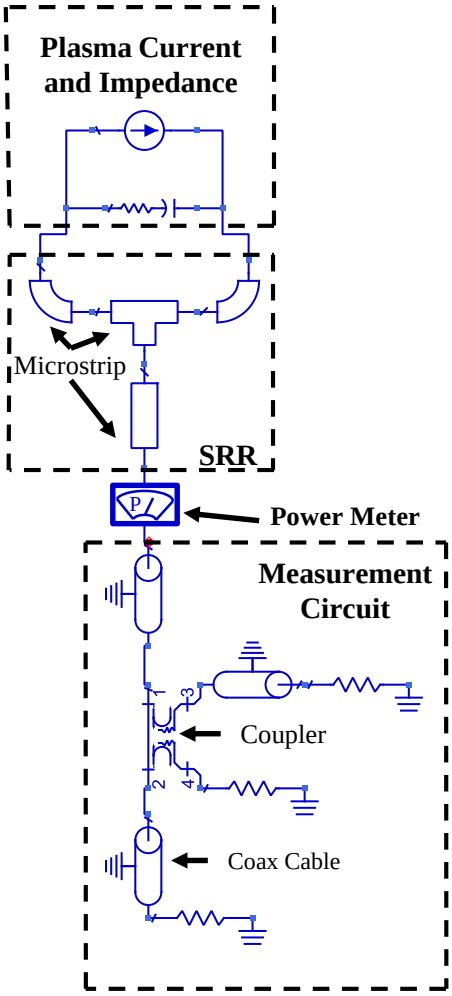

Figure 8.5. ADS circuit model for conversion of plasma current and impedance from fluid model for comparison with experimental power measurements

The SRR is modeled in ADS by means of two curved sections of microstrip transmission lines with a radius of 8.5 mm connected at one end using a T-junction. To create the input offset of 12°, one section has angle of 168° while the other section has an angle of 192°, for a combined angle of a complete ring (360°). The length of the discharge gap is small in comparison to the overall arc length of the

split ring and is neglected. A straight section of microstrip is added to the T-junction to simulate the input section for the split ring device.

The plasma current and impedance section of the circuit model consist of a current source to represent the third harmonic current produced by the plasma as well as resistance and capacitive element to represent the plasma impedance. For the ADS simulation, the third harmonic plasma current values were obtained from the FFT of the plasma current supplied by the fluid model. The plasma impedance values are deduced from the applied voltage at the electrode as well as the resulting fundamental current (obtained from the FFT of the total current). The values of the plasma capacitance and resistance are assumed consistent for both the fundamental and third harmonic frequencies. The values of harmonic current and plasma impedance vary depending on the net power and gas pressure used for the fluid model. Typically, the capacitance is between 0.1 and 0.3 pF, resistance between 0.3 and 1.2 kΩ, depending on the given gas pressure and net power to the plasma.

Figure 8.6 includes the experimental pressure sweep results. Also included are the fluid model 3rd harmonic current after conversion into 3rd harmonic power by the ADS circuit model. For proper comparison, net power measurements from the experiment were used as input into the fluid model, and are included for reference. This is an important step due to the experiment being run at a constant forward power, which means the net power changed during the course of the pressure sweep due to the changing plasma conditions. The modeled results are in reasonable agreement given the complexity of the problem. Both experimental and modeled results show peak harmonic generation at low pressure which then rapidly

decreases with pressure. As discussed in the experimental pressure sweep results in section 7, the rapid decrease in harmonic output is partially due to the reduction of asymmetry caused by condensing of the plasma around the discharge hap at increasing pressures, and applies to both the experiment and the model.

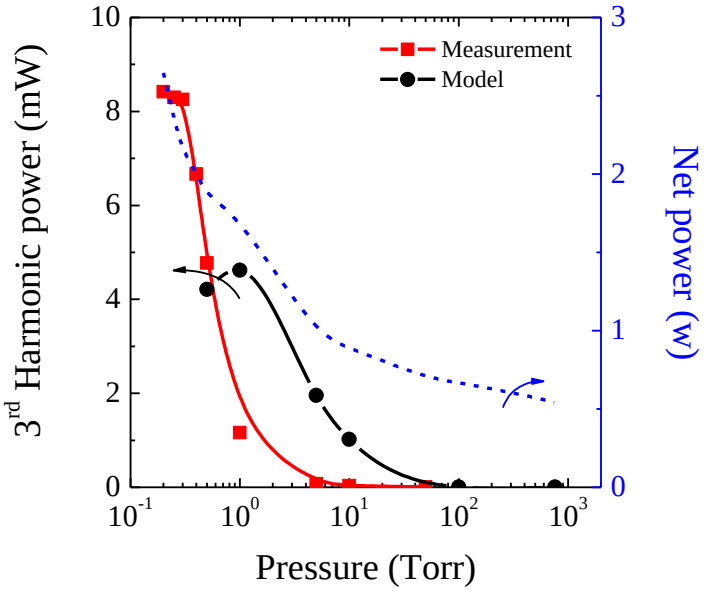

Figure 8.6. Measured 3rd harmonic (red-squares) and modeled 3rd harmonic (black-circles) as a function of gas pressure. Measured net power used for fluid model is shown in blue. [42]

A comparison 3rd harmonic output with experimental and modeled data is shown in Figure 8.7. Experimental data is the same as shown in Figure 7.4 for the fully asymmetric case (110:1 ratio). Data was taken at 0.3 Torr, which produces the peak harmonic output. Modeled data was taken at with the same electrode area ratio (110:1) and at a pressure of 10 Torr, which is the pressure of peak current output from the fluid model simulations (Figure 8.3). Due to the differences in plasma conditions for the experimental and modeled curves, a firm conclusion cannot be

attributed to this figure. However, in both cases it is clear that significant 3rd harmonic power can be obtained and has a strong dependence on the net input power applied to the plasma.

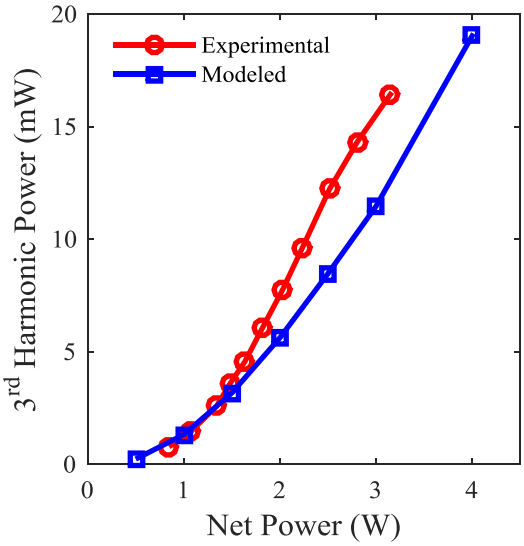

Figure 8.7. Comparison of experimental and modeled as a function of net input power to plasma. Experimental data (red-circles) taken in 0.3 Torr of argon. Modeled data (blue-squares) taken in 10 Torr.

9. Conclusion

An investigation of the nonlinearities in microplasmas reveal two key properties, nonlinear sheath motion, and nonlinear electron current. The nonlinear properties of the plasma need to be exploited in order to maximize the harmonic output to create an efficient frequency multiplier. Three key design considerations where shown to be electrode asymmetry, gas pressure, and net absorbed power.

According the equations developed, maximizing harmonic output requires asymmetric discharge areas. This is confirmed in both the experiments performed

and in the simulations of the fluid model. The asymmetry of the discharge plays a crucial role in the nonlinear displacement current through the sheath, which is the largest factor in creating harmonics. The small electrode has a smaller capacitance ($C_s = \epsilon A/d$), and as such requires an increase in voltage to maintain the current continuity ($I_d = C_s\, dV/dt$). This higher voltage strongly modulates the sheath width and induces nonlinearity in the sheath capacitance. Additionally the higher voltage generates hot electrons, which enhances the nonlinear electron current when the sheath width is at a minimum.

Based on both experiments and fluid model results, gas pressure mainly affects the electrode asymmetry. At low pressures, the plasma is allowed to expand to cover the electrodes in a manner that it was designed. However, at high pressures, the plasma constricts in size, and in the limiting case of 760 Torr, the electrodes become symmetric. At pressures below a certain point however, the plasma density is sufficiently low that harmonic output is reduced regardless of electrode asymmetry. These two phenomena create a maximum in harmonic output with pressure. This can be accounted for in future designs by reducing the size of the smallest electrode to take advantage of higher electron densities at higher pressures without loss of asymmetry.

Net absorbed power is also confirmed by both experiment and simulation to have a nonlinear relationship with harmonic output. Increasing input power to the plasma increases the voltage to the electrodes and thus increases the energy of the electrons. The higher energy electrons cause an increase to the nonlinear electron current. In the physical design of a system, increasing input power to the system

has unintentional consequences just as in semiconductor devices. While the plasma itself is able to absorb additional power, the microstrip substrate and metal electrodes will begin to erode and breakdown over time. Using substrate and electrode materials that can withstand higher temperatures, such as quartz and tungsten, can allow more power that what was experimentally available.

10. Future Work

Using the knowledge gained from the preceding work, additional modifications and studies can be performed in order to maximize the harmonic output of the SRR. Specifically, an efficient harmonic extraction method will need to be developed.

Studies in the microwave range of frequencies allow for ease of design and assembly of harmonic frequency multiplier devices. However, frequency multipliers in the microwave regime are of little interest as microwave frequencies can be readily created using various oscillator designs. For this reason, work has begun to utilize plasmas as a non-linear source in the mm-wave regime where frequency multipliers are still required as a source of power. A proposed system utilizes a conventional solid-state source of 45 GHz power in waveguide to generate a plasma. The goal of this system is to produce the third harmonic of 135 GHz with efficient extraction. There is little data available for either conventional plasmas or microplasma is this frequency range. As such, a significant study of the plasma parameters (such as density and temperature) and behaviors will need to be conducted.

11. References

[1] T. Löffler, K. Siebert, S. Czasch, T. Bauer, and H. G. Roskos, "Visualization and classification in biomedical terahertz pulsed imaging," *Phys. Med. Biol.*, vol. 47, no. 21, pp. 3847–3852, Nov. 2002.

[2] M. C. Beard, G. M. Turner, and C. A. Schmuttenmaer, "Terahertz Spectroscopy," *J. Phys. Chem. B*, vol. 106, no. 29, pp. 7146–7159, Jul. 2002.

[3] G. Chattopadhyay, "Technology, Capabilities, and Performance of Low Power Terahertz Sources," *IEEE Trans. Terahertz Sci. Technol.*, vol. 1, no. 1, pp. 33–53, Sep. 2011.

[4] M. Uenohara, M. Uenohara, T. Masutani, and K. Inada, "A new high-power frequency multiplier," *PROCEEDINGS OF THE INSTITUTE OF RADIO ENGINEERS*, vol. 45, no. 10. pp. 1419–1420, 1957.

[5] J. R. Baird and P. D. Coleman, "Frequency Conversion in a Microwave Discharge," *Proc. IRE*, vol. 49, no. 12, 1961.

[6] R. A. Stern, "Harmonic generation and frequency mixing at plasma resonance," *Phys. Rev. Lett.*, vol. 14, no. 14, p. 538, 1965.

[7] J. E. S. Asmussen and J. B. Beyer, "Microwave Harmonic Generation in a Plasma Capacitor," *IEEE Transactions on Electron Devices*. 1969.

[8] A. M. Bilgic, U. Engel, E. Voges, M. Kückelheim, and J. A. C. Broekaert, "A new low-power microwave plasma source using microstrip technology for atomic emission spectrometry," *Plasma Sources Sci. Technol.*, vol. 9, no. 1, pp. 1–4, Feb. 2000.

[9] F. Iza and J. a. Hopwood, "Low-power microwave plasma source based on a microstrip split-ring resonator," *IEEE Trans. Plasma Sci.*, vol. 31, no. 4, pp. 782–787, 2003.

[10] J. Kim and K. Terashima, "2.45 GHz microwave-excited atmospheric pressure air microplasmas based on microstrip technology," *Appl. Phys. Lett.*, vol. 86, no. 19, p. 191504, May 2005.

[11] F. Iza and J. Hopwood, "Split-ring resonator microplasma: microwave model, plasma impedance and power efficiency," *Plasma Sources Sci. Technol.*, vol. 14, pp. 397–406, 2005.

[12] J. J. Narendra, T. A. Grotjohn, and J. Asmussen, "Microstripline applicators for creating microplasma discharges with microwave energy," *Plasma Sources Sci. Technol.*, vol. 17, no. 3, p. 035027, Aug. 2008.

[13] J. L. Hesler, T. W. Crowe, and R. M. Weikle, "A 5 mW and 5% efficiency 210 GHz InP-based heterostructure barrier varactor quintupler," *IEEE Microw. Wirel. Components Lett.*, vol. 14, no. 4, pp. 159–161, Apr. 2004.

[14] T. W. Crowe, W. L. Bishop, D. W. Porterfield, J. L. Hesler, and R. M.

Weikle, “Opening the terahertz window with integrated diode circuits,” *IEEE J. Solid-State Circuits*, vol. 40, no. 10, pp. 2104–2110, Oct. 2005.

[15] S. M. Nilsen, H. Gronqvist, H. Hjelmgren, A. Rydberg, and E. L. Kollberg, “Single barrier varactors for submillimeter wave power generation,” *IEEE Trans. Microw. Theory Tech.*, vol. 41, no. 4, pp. 572–580, Apr. 1993.

[16] M. A. Lieberman, “Analytical solution for capacitive RF sheath,” *IEEE Trans. Plasma Sci.*, vol. 16, no. 6, pp. 638–644, 1988.

[17] M. A. Lieberman, “Dynamics of a collisional, capacitive RF sheath,” *IEEE Trans. Plasma Sci.*, vol. 17, no. 2, pp. 338–341, Apr. 1989.

[18] A. Iwai, Y. Nakamura, and O. Sakai, “Enhanced generation of a second-harmonic wave in a composite of metamaterial and microwave plasma with various permittivities.,” *Phys. Rev. E. Stat. Nonlin. Soft Matter Phys.*, vol. 92, no. 3, p. 033105, Sep. 2015.

[19] Y. Nakamura, A. Iwai, and O. Sakai, “Nonlinear properties of negative-permittivity microwave plasmas embedded in metamaterial of macroscopic negative permeability,” *Plasma Sources Sci. Technol.*, vol. 23, no. 6, p. 064009, 2014.

[20] H. R. Askari and Z. Azish, “Effect of a periodic magnetic field on phase matching condition in second harmonic generation at interactions of laser-plasma,” *Opt. - Int. J. Light Electron Opt.*, vol. 122, no. 13, pp. 1159–1163, Jul. 2011.

[21] P. Jha, R. K. Mishra, G. Raj, and A. K. Upadhyay, “Second harmonic generation in laser magnetized–plasma interaction,” *Phys. Plasmas*, vol. 14, no. 5, p. 053107, May 2007.

[22] K. P. Singh, D. N. Gupta, S. Yadav, and V. K. Tripathi, “Relativistic second-harmonic generation of a laser from underdense plasmas,” *Phys. Plasmas*, vol. 12, no. 1, p. 013101, Nov. 2005.

[23] E. Takahashi, M. Mori, N. Yugami, Y. Nishida, and K. Kondo, “Observation of the second-harmonic generation from relativistically quivering electrons in exciting laser wakefield.,” *Phys. Rev. E. Stat. Nonlin. Soft Matter Phys.*, vol. 65, no. 1 Pt 2, p. 016402, Jan. 2002.

[24] D. T. Young and J. C. Irvin, “Millimeter frequency conversion using Au-n-type GaAs Schottky barrier epitaxial diodes with a novel contacting technique,” *Proc. IEEE*, vol. 53, no. 12, pp. 2130–2131, 1965.

[25] E. Schlecht, F. Maiwald, and G. Chattopadhyay, *Design considerations for heavily-doped cryogenic Schottky diode varactor multipliers*. 12th International Sympossium on Space Terahertz Technology, 2001.

[26] J. V Siles, B. Thomas, G. Chattopadhyay, A. Maestrini, C. Lee, E. Schlecht, C. Jung, and I. Mehdi, “Design of a high-power 1.6 THz Schottky tripler using ‘on-chip’power-combining and Silicon micromachining,” in

Proceedings of 22 nd International Symposium on Space Terahertz Technology, Tucson, 2011, pp. 26–28.

[27] J. V. Siles, C. Lee, R. Lin, G. Chattopadhyay, T. Reck, C. Jung-Kubiak, I. Mehdi, and K. B. Cooper, "A High-Power 105–120 GHz Broadband On-Chip Power-Combined Frequency Tripler," *IEEE Microw. Wirel. Components Lett.*, vol. 25, no. 3, pp. 157–159, Mar. 2015.

[28] A. Maestrini, J. S. Ward, J. J. Gill, B. Thomas, R. H. Lin, G. Chattopadhyay, and I. Mehdi, "A Frequency-Multiplied Source With More Than 1 mW of Power Across the 840–900-GHz Band," *IEEE Trans. Microw. Theory Tech.*, vol. 58, no. 7, pp. 1925–1932, Jul. 2010.

[29] E. Kollberg and A. Rydberg, "Quantum-barrier-varactor diodes for high-efficiency millimetre-wave multipliers," *Electron. Lett.*, vol. 25, no. 25, p. 1696, Dec. 1989.

[30] J. R. Jones, G. B. Tait, S. H. Jones, and D. S. Katzer, "DC and large-signal time-dependent electron transport in heterostructure devices: an investigation of the heterostructure barrier varactor," *IEEE Trans. Electron Devices*, vol. 42, no. 6, pp. 1070–1080, Jun. 1995.

[31] L. Dillner, J. Stake, and E. L. Kollberg, "Analysis of symmetric varactor frequency multipliers," *Microw. Opt. Technol. Lett.*, vol. 15, no. 1, pp. 26–29, May 1997.

[32] J. Stake, T. Bryllert, A. O. Olsen, and J. Vukusic, "Heterostructure Barrier Varactor Quintuplers for Terahertz Applications," in *2008 European Microwave Integrated Circuit Conference*, 2008, pp. 206–209.

[33] J. Vukusic, T. Bryllert, T. Arezoo Emadi, M. Sadeghi, and J. Stake, "A 0.2-W Heterostructure Barrier Varactor Frequency Tripler at 113 GHz," *IEEE Electron Device Lett.*, vol. 28, no. 5, pp. 340–342, May 2007.

[34] Q. Xiao, J. L. Hesler, T. W. Crowe, B. S. Deaver, and R. M. Weikle, "A 270-GHz Tuner-Less Heterostructure Barrier Varactor Frequency Tripler," *IEEE Microw. Wirel. Components Lett.*, vol. 17, no. 4, pp. 241–243, Apr. 2007.

[35] A. Malko, T. Bryllert, J. Vukusic, and J. Stake, "Silicon Integrated InGaAs/InAlAs/AlAs HBV Frequency Tripler," *IEEE Electron Device Lett.*, vol. 34, no. 7, pp. 843–845, Jul. 2013.

[36] T. Bryllert, A. Malko, J. Vukusic, and J. Stake, "A 175 GHz HBV Frequency Quintupler With 60 mW Output Power," *IEEE Microw. Wirel. Components Lett.*, vol. 22, no. 2, pp. 76–78, Feb. 2012.

[37] J. Vukusic, T. Bryllert, Ø. Olsen, J. Hanning, and J. Stake, "Monolithic HBV-Based 282-GHz Tripler With 31-mW Output Power," *IEEE Electron Device Lett.*, vol. 33, no. 6, pp. 800–802, Jun. 2012.

[38] A. Malko, T. Bryllert, J. Vukusic, and J. Stake, "A 474 GHz HBV Frequency Quintupler Integrated on a 20 um Thick Silicon Substrate," *IEEE Trans.*

Terahertz Sci. Technol., vol. 5, no. 1, pp. 1–7, 2014.

[39] M. A. Lieberman and A. J. Lichtenberg, *Principles of Plasma Discharges and Materials Processing: Second Edition*. 2005.

[40] D. M Pozar, *Microwave Engineering*. 2012.

[41] A. R. Hoskinson and J. Hopwood, "Spatially resolved spectroscopy and electrical characterization of microplasmas and switchable microplasma arrays," *Plasma Sources Sci. Technol.*, vol. 015024, 2014.

[42] J. Gregório, S. Parsons, and J. Hopwood, "Microwave Harmonic Generation in Microplasmas," *Plasma Sources Sci. Technol*., submitted Jan. 2016

[43] J. Gregório, A. R. Hoskinson, and J. Hopwood, "Modeling of microplasmas from GHz to THz," *J. Appl. Phys.*, vol. 118, no. 8, 2015.